Volume 9
Number 1
January 2024
Pages 1–176

Nanoscale Horizons

The home for rapid reports of exceptional significance in nanoscience and nanotechnology

rsc.li/nanoscale-horizons

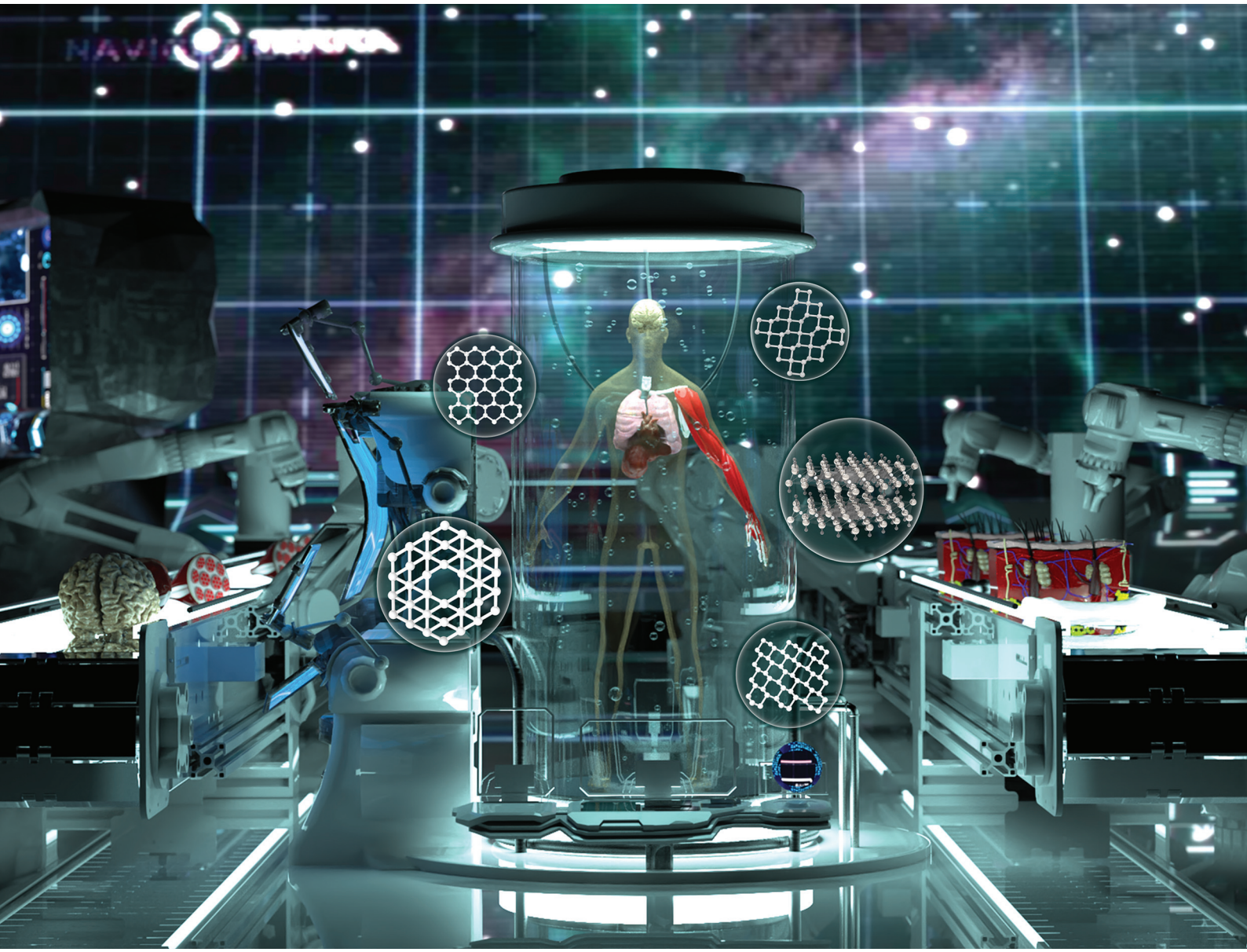

ISSN 2055-6756

ROYAL SOCIETY OF CHEMISTRY

REVIEW ARTICLE

Dong-Wook Han *et al.*

MXene and Xene: promising frontier beyond graphene in tissue engineering and regenerative medicine

NCNST

Nanoscale Horizons

REVIEW

View Article Online
View Journal | View Issue

Cite this: *Nanoscale Horiz.*, 2024, 9, 93

MXene and Xene: promising frontier beyond graphene in tissue engineering and regenerative medicine

Moon Sung Kang,†[a] Hee Jeong Jang,†[a] Hyo Jung Jo,[a] Iruthayapandi Selestin Raja[b] and Dong-Wook Han *[ab]

The emergence of 2D nanomaterials (2D NMs), which was initiated by the isolation of graphene (G) in 2004, revolutionized various biomedical applications, including bioimaging and -sensing, drug delivery, and tissue engineering, owing to their unique physicochemical and biological properties. Building on the success of G, a novel class of monoelemental 2D NMs, known as Xenes, has recently emerged, offering distinct advantages in the fields of tissue engineering and regenerative medicine. In this review, we focus on the comparison of G and Xene materials for use in fabricating tissue engineering scaffolds. After a brief introduction to the basic physicochemical properties of these materials, recent representative studies are classified in terms of the engineered tissue, *i.e.*, bone, cartilage, neural, muscle, and skin tissues. We analyze several methods of improving the clinical potential of Xene-laden scaffolds using state-of-the-art fabrication technologies and innovative biomaterials. Despite the considerable advantages of Xene materials, critical concerns, such as biocompatibility, biodistribution and regulatory challenges, should be considered. This review and collaborative efforts should advance the field of Xene-based tissue engineering and enable innovative, effective solutions for use in future tissue regeneration.

Received 26th September 2023,
Accepted 13th November 2023

DOI: 10.1039/d3nh00428g

rsc.li/nanoscale-horizons

Introduction

Recently, interest in 2D nanomaterials (2D NMs) has increased owing to their potential applicability in a wide range of biomedical fields.[1] It began when André Geim and Kostya Novoselov successfully isolated graphene (G) in 2004,[2] and subsequently, derivatives of G, such as G oxide (GO) and reduced GO (rGO), with numerous functional groups and lattice defects, were introduced.[3–5] The G derivatives have garnered significant attention in the biomedical field, particularly in bioimaging,[6,7] -sensing,[8,9] and -robotics,[14–16] theranostics,[10,11] drug delivery,[12] and tissue engineering,[13] owing to their special physicochemical and biological properties. The application of G in the fields of tissue engineering and regenerative medicine has enabled the tailoring of the biological and mechanical properties of native materials by introducing binding sites for further bio-functionalization with biological molecules. Additional properties, such as conductivity for regulating cell behavior, proliferation, and differentiation, which promote specific tissue regeneration, may also be introduced.[17–19]

Notably, extensive research on G enabled the development of other functional 2D NMs. The remarkable progress reported with respect to G over the past few decades has led to novel categories of functional 2D NMs, *i.e.*, transition metal dichalcogenides, transition metal oxides, layered double hydroxides, hexagonal BN, and metal–organic frameworks.[20] MXenes, which are 2D NMs comprising transition metal carbides and nitrides, were first discovered by Gogotsi *et al.* in 2011.[21] They exhibit remarkable features in converting photothermal energy, rendering them well-suited for applications in photonic hyperthermia treatment within the second near-infrared (NIR) biowindow (NIR-II biowindow), facilitating deep tissue penetration.[22,23] The range of metals available for use within MXenes renders them useful contrast agents in computed tomography (CT) and magnetic resonance imaging. The remarkable electrical conductivity and numerous functional groups of MXenes, which are highly promising for use in the fields of tissue engineering and regenerative medicine, merit attention in this regard.[24–27]

Subsequently, a novel category of monoelemental 2D materials emerged, known as Xenes. The component elements

[a] *Department of Cogno-Mechatronics Engineering, College of Nanoscience and Nanotechnology, Pusan National University, Busan 46241, Republic of Korea. E-mail: nanohan@pusan.ac.kr*
[b] *BIO-IT Fusion Technology Research Institute, Pusan National University, Busan 46241, Republic of Korea*
† These authors contributed equally to the paper.

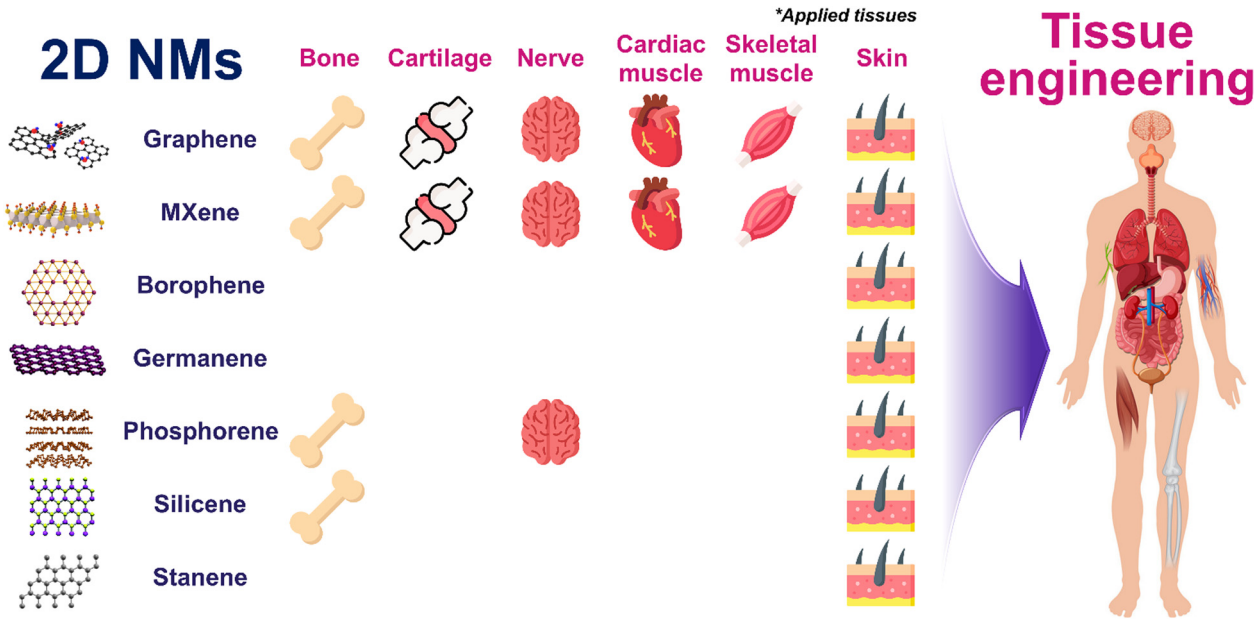

Fig. 1 Schematic of Xene materials for use in various tissue engineering and regeneration.

primarily occur in the main groups of the periodic table, *i.e.*, IIIA (B, Al, Ga, and In), IVA (Si, Ge, Sn, and Pd), VA (P, As, Sb, and Bi), and VIA (Se and Te).[28] Following a nomenclature akin to that of G, these monoelemental 2D materials are typically named by combining the elemental names with the suffix "-ene," yielding names such as borophene, germanene, and tellurene. Xenes exhibit rapid responses to external stimuli (*e.g.*, NIR laser irradiation or pH changes) owing to their ultrathin 2D structures.[29] This enables the triggered and/or controlled release of loaded molecules, rendering them suitable for use in the targeted delivery of multi-responsive therapeutics to desired sites.[30] Additionally, the chemical properties of Xenes, including their tunable, versatile surface chemistries, enable the adsorption of various biomolecules, proteins, and cyto-/chemokines, facilitating regenerative medicinal applications.[31–33]

In this review, we explore the emerging era of MXenes and other types of Xene materials that display potential for use in the fields of tissue engineering and regenerative medicine (Fig. 1). We analyze the distinctive attributes of Xenes, which surpass those of G, and their potential applications in engineering and restoring various tissues, including bone, cartilage, nerves, muscles, and skin. Moreover, we address the opportunities and challenges associated with the utilization of 2D NMs beyond G in the context of the future clinical and industrial applications of Xenes.

Classification and physicochemical characteristics of Xenes

This section provides a concise overview of commonly employed Xenes, including their synthetic techniques and typical features. Based on the positions of their elements in the periodic table, Xenes may be classified as follows: Group III (borophene and gallenene), Group IV (silicene, germanene, and stanene), Group V (phosphorene, arsenene, antimonene, and bismuthene), and Group VI (selenene and tellurene).[29]

G derivatives

G serves as a representative 2D NM and displays numerous structural features characteristic of 2D NMs. Its structure comprises a single layer of C atoms covalently bonded in a flat, regular hexagonal pattern *via* sp^2 bonds.[34] Conversely, GO exhibits the same hexagonal C atom arrangement but contains sp^3 C atoms bonded to functional groups above or below the plane of the NM, resulting in a rougher structure, accompanied by pronounced local polarity. GO is a non-stoichiometric compound of C, O, and H in a variable ratio, which is influenced by the processing methods used. It contains abundant O-containing functional groups, including epoxide, carbonyl, hydroxyl, and phenol groups, which are introduced during chemical exfoliation.[35] These defects alter the inert G structure, resulting in unique properties that enable diverse applications as sensors, photovoltaics, membranes, purification materials, *etc.*[36] rGO lies in between G and GO in terms of structure. It may be produced by reducing GO *via* electrochemical, microwave, and photo-assisted thermal methods, which eliminate most functional groups and partially restore sp^2 hybridization.[37,38] rGO exhibits excellent light absorption characteristics across the entire spectrum, with even a single layer displaying the capacity to absorb a substantial amount of light at visible and NIR wavelengths.[39]

MXenes

MXenes are synthesized by selectively removing specific atomic layers from parent MAX materials using HF or a combination of

a potent acid and fluoride salt.[40] Their structural formula is $M_{(n+1)}X_nT_x$, with M representing early transition metals, such as Ti, V, Zr, and Nb, X representing C and/or N, and T representing surface functional groups, such as –O, –OH, and –F. Varying the atomic layer number in the unit cell yields the typical structures $M_{2X}T_x$, $M_3X_2T_x$, and $M_4X_3T_x$.[41] Initially, MXenes were investigated for use in energy conversion and storage systems due to their high theoretical capacity and electrical conductivity, but recently they have received significant attention in the field of photocatalysis.[42] Their exceptional physicochemical characteristics may be ascribed to several factors. Wet chemical etching generates an abundance of functional groups, facilitating close contact between the MXene and biological system or material.[43] Adjustments in surface chemistry enable the tuning of the bandgap alignment of the MXene. The conductive metal cores within the layered structure endow the MXene with excellent metallic conductivity and electron-accepting capacity. Consequently, MXenes emerged as strong candidates among 2D materials, and they have been thoroughly explored for use in various photocatalytic applications, including H_2O splitting, CO_2 reduction, pollutant degradation, and N_2 fixation.[42] Additionally, the simple surface modification of an MXene improves the *in vivo* performance by reducing toxicity, enhancing colloidal stability, and prolonging circulation within the body.[44]

Group III Xene (borophene)

B is one of the most chemically complex elements due to its trivalent electronic configuration.[45] This complexity disrupts the octet rule, resulting in an unusual electron-poor bonding pattern, where the electrons of B and its compounds are shared among ≥ 3 atoms.[46] In its bulk form, pure B exhibits significant structural diversity, with 5–16 different polymorphs with highly complex unit cells.[47] Borophene, which is a unique 2D B sheet, displays remarkable properties, including a tunable anisotropic structure, metallic behavior, optical transparency, and potential high-temperature superconductivity (10–20 K).[48–50] Various synthetic methods, such as physical vapor deposition (PVD), mechanical cleavage, etching, and liquid-phase exfoliation, have been successfully employed in producing borophene.[51,52]

Group IV Xenes (silicene, germanene, and stanene)

Silicene displays a non-planar buckled honeycomb configuration in its monolayer form, which is distinct from the sp^2-hybridized C atoms within bulk graphite.[53] It should exhibit G-like Dirac fermions and semi-metallic properties, along with enhanced spin–orbit coupling effects due to its lower symmetry.[54,55] Theoretical insights suggest that silicene may exhibit topologically nontrivial electronic states, gate-tunable bandgaps, and spin-polarized edge states, rendering it suitable for use in devices such as tunable transistors and photodetectors.[56] Experimental synthetic methods, such as PVD and chemical exfoliation, have been successfully employed in producing silicene.[57] Germanene, akin to silicene, features a buckled honeycomb structure,[58] which is characterized by Ge atoms forming a corrugated 2D layer structure, driven by its enhanced spin–orbit coupling due to its heavier atomic nature compared to that of Si.[59] This attribute endows germanene with stronger topological insulator properties. Common methods of synthesizing germanene include mechanical cleavage and PVD.[60] Similar to silicene and germanene, stanene displays a buckled honeycomb lattice structure with stable $\pi\cdots\pi$ bonding within the atomic plane.[61] The distinct feature of stanene is its strong spin–orbit coupling, which deviates from the behavior of graphene and results in a bandgap opening of approximately 0.1 eV, with topologically nontrivial states at the edges of the material.[62] Stanene, which is a promising topological insulator, has been experimentally synthesized using PVD.[63]

Group V Xene (phosphorene)

P exhibits various allotropes, including gaseous P, black P (BP), blue P, white P, violet P, and red P. BP, which is the most thermodynamically stable allotrope, has been studied extensively, particularly its 2D variant, referred to as phosphorene. Phosphorene exhibits an orthorhombic structure characterized by parallel atomic layers that are puckered in a double-floor arrangement.[64] Every P atom within an atomic layer bears 5 valence electrons and engages in covalent bonding with adjacent P atoms.[65] At an elevated pressure, BP displays the capacity to undergo transition to a semi-metallic β phase, which is characterized by a double-layered rhombohedral structure comprising ruffled, interlocked, six-membered rings.[64,66] Due to its versatility, BP is one of the most studied Xenes after G, and various experimental methods have been developed for use in phosphorene synthesis, including mechanical cleavage,[67] liquid-phase exfoliation,[68] etching,[69] chemical vapor deposition,[70] PVD,[71] and wet-chemistry techniques.[72]

Tissue regeneration using MXenes and Xenes: comparison with G derivatives

Bone and cartilage tissue engineering using G, MXenes, and Xenes

Bone tissue engineering. In recent decades, G and its derivatives (GO and rGO) have been extensively employed in bone and cartilage tissue engineering (Table 1). rGO, in particular, has residual functional groups that render it more biocompatible than pristine G.[73,74] Furthermore, its characteristic structural defects and O-containing functional groups provide sites for potential bioconjugation and interaction with biological molecules, rendering rGO a superior choice for interfacing with biological systems.[75] Kang *et al.* studied the fabrication of rGO-coated Ti (rGO-Ti) substrates for use in orthopedic and dental tissue regeneration (Fig. 2a–e).[76] These substrates were fabricated using meniscus-dragging deposition to introduce a robust, uniform rGO coating layer. The R_q values of the rGO-Ti substrates were lower than that of intact Ti, indicating significantly flattened surfaces with microscale grooves. An *in vitro* assay using human mesenchymal stem cells (hMSCs) showed that the rGO-Ti substrates significantly increased cell proliferation after 7 days (d) of incubation.

Table 1 G, MXene, and Xene-based tissue engineering approaches for use in bone regeneration

Applications	Xene materials	Formulations	Test species	Biocompatibility and therapeutic applications	Enhanced osteogenic markers	Outlooks	Ref.
Bone	rGO	rGO-Ti substrate	hMSCs	High viability at 4 mg mL^{-1} rGO-coated substrates	ALP Mineralization nodule formation	Osteogenic properties of rGO can be applied for dental and orthopedic bone implants	76
	GO	GO-Alg/Gel hydrogel	hMSCs	90% viability at 2 mg mL^{-1} Enhanced spreading and proliferation for 42 d	COL1A2, SOST, ALP, BGLAP, and PHEX Mineralization nodule formation Stress fiber expression	Potential *ex vivo* model for critical-sized defects	97
		PGBC nanocomposites	SD rat primary osteoblasts	95–100% viability at 0.5 w/w%	ALP, OPN, and Smad5	Viable orthopaedic materials for clinical application	78
			New Zealand rabbit	Sustained attachment and proliferation with no apoptosis during 7 d No hematological toxicity	BV/TV, TbN, TbSp		
		GO-coated PLA film	MC3T3-E1 cells	82% viability at 0.1 mg mL^{-1} Enhanced migration, adhesion, spreading, and proliferation for 5 d High membrane integrity with no intracellular ROS generation	Bone mineral density BV/TV, Tb.Th, Tb.Sp, and Tb.N	Customizable structured GBR implant for dental regeneration	98
	Nb_2C MXene	3DP NBGS lattices	Saos-2 cells	90% cell viability at 1 mg mL^{-1} NIR-radiated photonic hypothermia	NIR-assisted tumor suppression Neovascularization Col1, OCN, RUNX2, and OPN BV/TV, BMD, and lowered porosity	Photothermal properties in the NIR-II biowindow offer effective treatment of bone malignancy and osteosarcoma	79
	$Ti_3C_2T_x$ MXene	MXene films	MC3T3-E1 cells	Enhanced adhesion, actin filament spreading, and proliferation on free-standing MXene films No noticeable inflammatory cell infiltration and necrosis	ALP, OCN, and OPN Bone volume fracture, Tb.Th, and Tb.Sp New bone volume	Biocompatibility, osteoinductivity, and osseointegration of MXene NPs are highlighted for GBR therapy	80
		MXene/RSF hydrogels	BMSCs	MXene < 8 mg mL^{-1} was cytocompatible	RUNX-2, Col-1, OCN, COL-1, and ALP	Piezoresistive and electroactive properties promote direct osteogenesis by activating the Ca^{2+}/CALM signaling pathway	81
			RAW264.7 cells	MXene supported angiogenesis, upregulation of immune regulatory markers with M2 polarization	Ca^{2+}/CALM signaling pathway		
			HUVECs Sprague–Dawley rats	ES enhanced neovascularization and macrophage polarization			
	BP	BP-CNTpega injectable gel	MC3T3-E1 cells	No cell viability at 0.4 mg mL^{-1} BP	ALP and OCN	Enhanced mechanical strength, electrical conductivity, and continuous phosphate ion release for bone regeneration therapy	85
			Rabbits	Enhanced adhesion and proliferation ES supported osteogenesis and cell growth both *in vitro* and *in vivo*	CSF-1, GDF10, VEGF-A, SMAD1, CSF3, NOG, and INTB1 Osseointegration in bone defects		
		BP-GelMA/U-Arg-PEA hydrogel	hDPSCs	No significant cytotoxicity up to 300 mg mL^{-1}	Col1, BMP4, and RUNX2	Supplying extra phosphorus for effective bone regeneration	86
			New Zealand rabbits	Supported cell adhesion, spreading, and migration	Accelerated new bone formation ALP and mineralization nodule formation		
		BP/GelMA-CaP hydrogel	hMSCs Saos-2 cells SD rats	No cytotoxicity up to 0.1 w/v% BP NIR-assisted anti-bacterial effects	RUNX2, ALP, OCN, and OPN ALP and mineralization nodule formation BMD, BV/TV, and BV New bone formation	Multifunctional therapeutic BP nanocomposite offering photothermal antibacterial capability and bone regeneration	87

Table 1 (*continued*)

Xene materials	Formulations	Test species	Biocompatibility and therapeutic applications	Enhanced osteogenic markers	Outlooks	Ref.
Silicene	SNSs@AIPH/CPC scaffold	BMSCs	No cytotoxicity up to 29 μmol mL^{-1}	ALP and mineralization nodule formation	Thermodynamic properties under NIR-II irradiation promoting sequential and multistage bone regeneration	93
		HUVECs	NIR radiation promoted proliferation and angiogenesis	OPN, BSP, RUNX2, OXS		
		SD rats		Lama5, Tgfb3, Col15a1, Fgf10, Ramp1, Bmp2, Smad3, Bmp6, Wnt5b, Sema3a, and Smad1		
				New bone formation with enhanced BMD, BV/TV, and Tb.N		
	H-Si TCP scaffold	BMSCs	ROS scavenging effects	SP7, BMP2, SPP1, and ALP	Orchestrating scaffold degradation and bone regeneration in a spatiotemporal manner through osteoimmunomodulation for treating large bone defects	94
		Raw264.7 cells	No cytotoxicity up to 50 μg mL^{-1}	TGFβ and BMP signaling pathway		
		SD rats	Supported adhesion and proliferation of BMSCs	Mineralization nodule formation		
			Immunoregulatory effects on Raw264.7 and M2 polarization	New bone formation with less fibrous encapsulation and more osseous tissue accumulation		
	H-Si@HAp-Ti	BMSCs	ROS scavenging and autophagy activation	SOD1, OCN, OPN, and OSX	Fracture healing by regulating the acidic microenvironment suppressing oxidative stress and facilitating osteogenic differentiation	96
		MC3T3-E1 cells	No hemotoxicity	ALP activity and mineralization		
		SD rats	Supported cell adhesion and proliferation up to 1.2 mg mL^{-1}	Osseointegration with enhanced BMD and BV/TV		

Furthermore, the rGO-Ti substrates significantly promoted alkaline phosphatase (ALP) activity and matrix mineralization, which are respective markers of early- and late-stage differentiation. Therefore, these substrates may be effectively utilized as dental and orthopedic bone substitutes due to their superior bioactivities and osteogenic potential and potent effects in stimulating the osteogenic differentiation of hMSCs. Meanwhile, 3D printing methods enable the fabrication of scaffolds with more precise designs, enabling the emulation of the 3D microenvironments of natural extracellular matrices (ECMs). Multiple recent studies have utilized 3D printing to produce 3D scaffolds that encourage encapsulated cells to exhibit morphologies and characteristics closer to those of their *in vivo* states.[77] Zhang *et al.* introduced a GO-incorporated alginate (Alg) and gelatin (Gel) composite bioink (GO-Alg/Gel) for use in the 3D bioprinting of bone-mimicking scaffolds. The prepared bioinks with higher GO concentrations (0.5, 1, and 2 mg mL^{-1}) exhibited improved bioprintability, scaffold fidelity, compressive moduli, and cell viability. The bioink supported the osteogenic differentiation of hMSCs, with the upregulation of osteogenic-related gene expression, including ALPL, BGLAP, and PHEX. After 42 d of culture in a bioreactor, the hMSC laden constructs displayed high mineral volumes with enhanced proliferation and osteogenic differentiation. This highlights the potential of the GO-Alg/Gel composite bioink for use in fabricating engineered bone tissues and developing *in vitro* tissue/organ models for application in *ex vivo* studies. Tan *et al.* developed a bioactive GO-functionalized self-expandable hydrophilic osteogenic nanocomposite for use in orthopedic applications.[78] They added GO to self-expandable P(MMA-AA-St) polymers (PGBC nanocomposites) to reinforce their biomechanics and -activities. The PGBCs exhibited outstanding compressive strengths (>70 MPa) and levels of H_2O absorption and volume expansion, in addition to extended handling times and reduced setting temperatures. Micro-CT was used to analyze the porosity of the PGBCs; the results indicated enhanced levels of bone–PGBC contact and osteogenic capacity. *In vitro* studies indicated that the cytocompatibility of the PGBCs was superior to that of the commonly used poly(methyl methacrylate) bone cement, based on the cell counting kit-8 assay, live/dead cell staining, and flow cytometry. Osteoblasts extracted from Sprague–Dawley (SD) rats exhibited improved levels of adhesion to the PGBCs, and the levels of expression of ALP, osteopontin (OPN), and Smad5 were upregulated. *In vivo* studies using rabbits revealed the promising intraoperative handling properties, convenient implantation, and satisfactory biosafety of the PGBCs. Kang *et al.* used 3D printing to fabricate GO-incorporated polylactic acid (PLA) films for use in guided bone regeneration (GBR). The incorporation of GO into the PLA films significantly increased the film's hydrophilicity and levels of protein adsorption. Moreover, the GO-PLA films supported the viability, migration, and proliferation of MC3T3-E1 preosteoblasts, whereas no significant membrane damage or expression of intracellular reactive oxygen species (ROS) was observed. Micro-CT revealed that, after transplantation into a rat calvarial bone defect model, GO

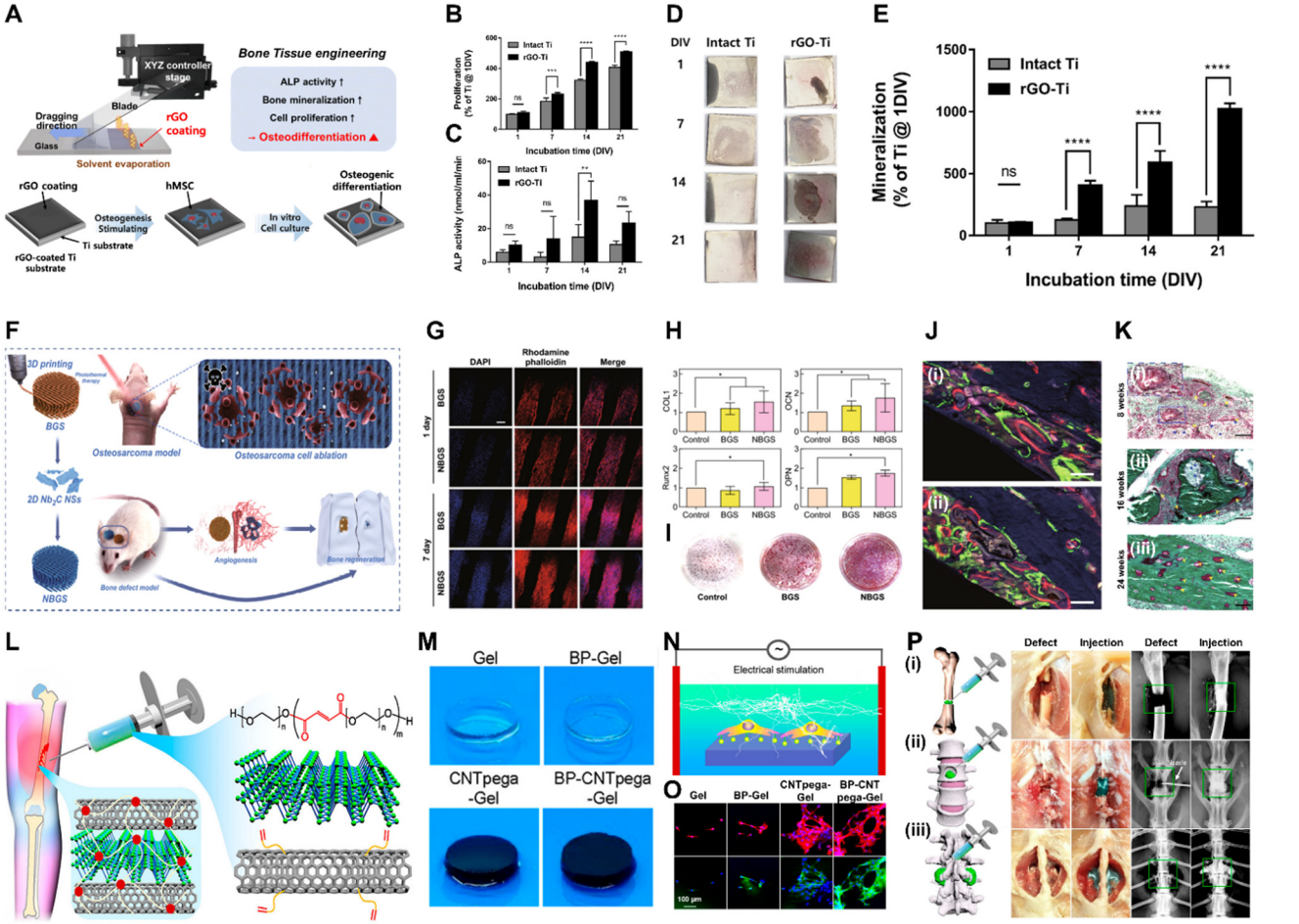

Fig. 2 Xene-based tissue engineering scaffolds for use in bone regeneration. (A)–(E) rGO-coated Ti substrates for use in osteogenic differentiation of hMSCs. (A) Fabrication of the rGO-Ti substrates. (B) Proliferation and (C) ALP activity of hMSCs within 21 d. (D) Digital images and (E) quantified results of the ARS staining of the hMSCs cultured on the rGO-Ti substrate within 21 d. Data reproduced from ref. 76. Copyright Springer Nature 2021. (F)–(K) 3DP NBGS lattices for use in osteosarcoma phototherapy and osteogenesis. (F) Fabrication and study scheme of the 3DP NBGS lattices. (G) Immunofluorescence-stained images of the hBMSCs on BGS/NBGS (blue: nucleus and red: F-actin). (H) Relative expression of osteogenic genes. (I) ARS staining of hBMSCs cultured on different groups. (J) New woven bone around the scaffold at wk 8 at spots (i) 1 and (ii) 2. (K) Goldner trichrome staining of the regenerated tissue in the NBGS group at wks (i) 8, (ii) 16, and (iii) 24. Data reproduced from ref. 79. Copyright Springer Nature 2021. (L)–(P) BP-CNTpega injectable gel for use in bone tissue engineering. (L) Schematic and (M) digital microscopy image of the fabricated BP-CNTpega gel. (N) Schematic and (O) immunofluorescence-stained images of ES-promoted cell proliferation. (P) Capacity of the injectable BP-CNTpega-gels to fill various bone defects. Photograph and X-ray images of rabbit (i) femur and (ii) vertebral body and (iii) posterolateral spinal fusion. Data reproduced from ref. 85. Copyright American Chemical Society 2020. The scale bars represent (J) 250, (G) and (K) 200, and (O) 100 μm, and the asterisks denote statistical significance (*$p < 0.05$, **$p < 0.01$, ***$p < 0.001$, ****$p < 0.0001$, and ns: not significant).

significantly improved the bone mineral density and volume fraction and trabecular thickness (Tb.Th), separation, and number (Tb.N), suggesting that the GO-PLA films act as barrier membranes in GBR.

Owing to their biofunctionalities, which are due to their numerous functional groups and elemental nature, MXene nanoparticles (NPs) were recently utilized in bone tissue engineering. Yin *et al.* developed Nb_2C MXene-functionalized scaffolds, which were combined with NIR-radiation osteosarcoma phototherapy in restoring bone defects *via* angio- and osteogenesis (Fig. 2F–K).[79] Bioactive glass (BGS) was reinforced with Nb_2C MXenes to fabricate NBGS bioinks. These Nb_2C-MXene nanosheets (NSs) exhibit unique photonic responses in the NIR-II biowindow, rendering them effective in killing bone cancer cells, with deep tissue penetration. Additionally, as the Nb-based components of the Nb_2C MXenes are degraded, they stimulate the growth and migration of blood vessels in the vicinity of the bone defect. This enhances the delivery of O_2, nutrients, and immune cells, accelerating scaffold degradation and providing space for bone remodeling. Furthermore, Ca and PO_4^{3-} released during scaffold degradation support the mineralization of new bone tissue. Therefore, the multimodal properties of the NBGS scaffolds may facilitate bone regeneration with anticancer effects, rendering them promising biomaterials for use in treating bone tumors. Zhang *et al.* assessed the biocompatibility and osteogenic potential of a $Ti_3C_2T_x$ MXene in

in vitro and *in vivo* settings to elucidate its suitability for use in bone tissue engineering.[80] They produced flexible MXene films using the MILD method and conducted *in vitro* and *in vivo* studies. *In vitro* studies using MC3T3-E1 cells revealed that the MXene films significantly enhanced early-stage osteogenic differentiation, as indicated by the increased ALP activity and expression of osteogenic genes. The subcutaneous implantation of the MXene films in rats demonstrated their excellent biocompatibility, with mild inflammatory responses and tissue integration. In a rat calvarial defect model, the MXene films adhered well to the bone tissue, whereas the positive control Ti membranes exhibited reduced mechanical compatibility over time. Micro-CT revealed that the MXene films promoted significant, uniform new bone formation in the defect area, which was guided by the films. Histological analysis confirmed mature bone regeneration on the MXene films without inflammatory reactions. Overall, this study provided valuable insights into the biocompatibility and osteoinductive properties of $Ti_3C_2T_x$ MXenes, thereby supporting their application in bone regeneration. In a study conducted by Hu *et al.*, a Ti_3C_2 MXene-incorporated regenerated silk fibroin (RSF) hydrogel was prepared and used in elucidating the role of electrical stimulation (ES) in bone regeneration.[81] ES accelerates the development, specialization, and multiplication of various cell types, including stem cells (SCs).[82] RSF, which is sourced from *Bombyx mori* silkworms, is an extensively studied biopolymer known for its exceptional mechanical strength, biocompatibility, and controllable biodegradability.[83] The MXene and ES enhanced osteogenic differentiation, based on increased ALP activity and Alizarin red S (ARS) staining, in addition to the upregulation of osteogenic markers (*i.e.*, runt-related transcription factor 2 (RUNX2), Col-1, osteocalcin (OCN), COL-1, and ALP) at the protein and messenger ribonucleic acid (mRNA) levels. ES also promotes M2 macrophage polarization and indirectly enhances the osteogenic differentiation of BMSCs. The MXene/RSF hydrogels combined with ES promoted neovascularization *in vitro*, enhancing the migration and tube formation capacity of human umbilical vein endothelial cells (HUVECs). Additionally, the use of MXene/RSF hydrogels resulted in significant levels of bone regeneration, mineralization, and angiogenesis in cranial defect models, with enhanced levels of M2 macrophage polarization, good biocompatibility, and gradual levels of degradation. Ribonucleic acid (RNA) sequencing indicated that ES upregulated genes related to biomineral tissue development and the Ca signaling pathway, particularly the CALM gene, suggesting that ES-induced osteogenic effects are associated with the activation of Ca^{2+}/CALM signaling within BMSCs.

BP is one of the most advantageous biomaterials for use in tissue engineering, because P is involved in various cell signal cascades, in addition to metabolism, membrane and nucleic acid structures, mineralized matrix formation, and enzyme catalysis.[84] Liu *et al.* engineered a BP-infused C nanotube-polyethylene glycol-acrylate (BP-CNTpega) injectable hydrogel for use in repairing irregular tissue defects by enhancing the mechanical strength, electrical conductivity, and PO_4^{3-} release to support bone tissue regeneration (Fig. 2L–P).[85] The BP-CNTpega hydrogel exhibited a PO_4^{3-} release profile with an initial burst release, followed by a slower release due to BP oxidation. Cell viability and proliferation were significantly enhanced within the nanocomposite gel, likely due to the endogenous PO_4^{3-} release and improved mechanical properties. ES was applied to enhance cellular growth and osteogenesis in MC3T3 preosteoblasts, leading to significantly increased levels of cell proliferation, ALP activity, OCN content, and expression of multiple osteogenic genes. The BP-CNTpega hydrogel effectively filled the defect sites in rabbit models, according to X-ray visualization, highlighting its potential for use in diverse bone defect repair applications. In a study conducted by Huang *et al.*, BP was incorporated into a photopolymerizable hydrogel comprising gelatin methacrylamide (GelMA) and cationic arginine-based unsaturated poly(ester amide)s (U-Arg-PEAs), denoted the BP-GelMA/U-Arg-PEA hydrogel.[86] The prepared hydrogels exhibited photoresponsive levels of PO_4^{3-} release upon exposure to 808 nm NIR irradiation and enhanced levels of *in vitro* mineralization and retained superior mechanical properties, even after 15 d of immersion in simulated body fluid. The BP-GelMA/U-Arg-PEA hydrogel stimulated the enhanced mineralization of human dental pulp SCs (hDPSCs). Western blot analysis and the enzyme-linked immunosorbent assay and reverse transcription quantitative polymerase chain reaction (rt-qPCR) confirmed elevated levels of osteogenic markers, such as Col-1, bone morphogenetic protein 4 (BMP4), and RUNX2, within the hDPSCs treated with BPN-containing hydrogels. This suggests that the presence of Ca-free P within these hydrogels was crucial in promoting osteogenic differentiation *via* the BMP–RUNX2 pathway. *In vivo* evaluation of rabbit calvarial defects demonstrated enhanced bone regeneration, leading to the formation of mature bone within 12 weeks (wk), as indicated by histological analysis, vascular formation, and the expression of osteogenic markers. Meanwhile, Miao *et al.* fabricated a BP/GelMA-CaP hydrogel *via* 3D printing and assessed its *in vitro* and *in vivo* osteogenic properties.[87] CaP reinforces crosslinked networks and enhances multiple bioactivities of hydrogels.[88,89] The BP/GelMA-CaP hydrogel displayed significant photothermal properties under NIR irradiation, leading to a substantial increase in temperature that diminished the activities and viability of Saos-2 osteosarcoma cells and *Staphylococcus aureus*. *In vitro* assays using hMSCs revealed significantly upregulated expression of osteogenesis-related genes, including OCN and OPN, and increased ALP activity. Immunofluorescence assays revealed increased expression of the RUNX2, ALP, OCN, and OPN proteins within the BP/GelMA-CaP hydrogel, and increased Ca deposition was observed using ARS staining. *In vivo* compatibility and therapeutic performance were assessed using a rat cranial defect model, which indicated excellent biocompatibility for subcutaneous implantation and significantly enhanced new bone formation, as revealed by micro-CT, histomorphometric analysis, and hematoxylin and eosin (H&E) staining.

Si, as the second most abundant element on Earth, is highly regarded for its biocompatibility. It is a key component in various nanomedicines and biomaterials due to its roles in collagen and elastin syntheses and its presence in essential bodily components, such as bone and hair.[90] Silicene exhibits exceptional characteristics, such as a large surface area and high biocompatibility, photothermal conversion in the NIR biowindow, and biodegradability, rendering it an attractive candidate for use in biomedical engineering.[91,92] In this context, Ni *et al.* engineered $Ca_3(PO_4)_2$ cement (CPC) containing SiO_2-silicene@2,2′-azobis(2-(2-imidazolin-2-yl) propane) (SNSs@AIPH/CPC), with inherent thermodynamic properties and osteoinductive activity.[93] *In vitro* studies using HUVECs revealed that SNSs@AIPH/CPC treatment with NIR-II irradiation led to increased cell proliferation, migration, and tube formation and the upregulation of vascular endothelial growth factor (VEGF). *In vivo* studies revealed denser vascular networks and enhanced VEGF expression around the bone defect sites after NIR-II irradiation. Additionally, SNSs@AIPH/CPC significantly enhanced the early-stage osteogenic differentiation and late-stage mineralization of BMSCs. High-throughput RNA sequencing and pathway analysis revealed that SNSs@AIPH upregulated genes associated with the tumor growth factor β and BMP signaling pathways, which are critical in osteogenesis. *In vivo* studies using a rat cranial defect model indicated that SNSs@AIPH/CPC-NIR-II exhibited outstanding osteoinductive properties, significantly improving the bone mineral density and volume and Tb.N compared to the other groups. Polychrome fluorescent labeling confirmed the strong osteogenic capacity, particularly with NIR-II activation, and immunohistochemical staining supported the enhancement of new bone formation. Lin *et al.* introduced a hydrogenated-Si NSs (H-Si NSs)-functionalized β-tricalcium phosphate (H-Si TCP) scaffold for use in healing bone defects.[94] Due to their capacity to scavenge excess ROS, the H-Si TCP scaffolds promoted M2 macrophage polarization, with up- and downregulation of the M2 and M1 markers, respectively. The H-Si TCP scaffolds upregulated the expression of key osteogenic markers, including BMP2, ALP, secreted phosphoprotein 1, and SP7, in the early and late stages of osteogenesis and promoted ALP activity and Ca deposition. This may be attributed to the sustained release of ionic Si, which activates osteogenic signaling pathways and supports biomineralization. *In vivo* studies revealed that the H-Si TCP scaffolds induced well-coordinated immune responses with reduced fibrous encapsulation, monocyte infiltration, and pathological fibrosis aided by foreign-body giant cells. *In vivo*, H-Si TCP significantly accelerated osteogenesis by promoting osteoblastic differentiation and activation, as indicated by the increased osteogenic activity and histological evidence of more activated osteoblasts, leading to the enhancement of new bone formation. It also significantly promoted bone remodeling by providing Ca, P, and Si, leading to improved bone repair and mineralization, as indicated by micro-CT and histological analysis of the improved bone volume and density and Tb.Th. Hydroxyapatite (HAp) exhibits the advantages of excellent biocompatibility and the capacity to integrate with natural bone tissue, rendering it a preferred material for use in bone implants and coatings.[95] Yuan *et al.* anchored 2D H-Si NSs onto HA-coated Ti substrates to develop H-Si@HAp-Ti implants.[96] The study investigated the influence of the H-Si@HA coating on BMSCs and MC3T3 cells, highlighting the role of Si ion release from the H-Si NSs in enhancing cell proliferation, osteogenic differentiation, and the expression of osteogenic markers. The results suggest that Si ions are critical in promoting osteogenic processes, including enhanced Ca deposition, activation of Wnt signaling, and ROS scavenging. The study investigated the *in vivo* osteogenesis and bone fracture-healing properties of H-Si@HA@Ti in a rat tibial fracture model. H-Si@HA@Ti significantly enhanced fracture healing, bone formation and mineral density, and the maximum bending load compared to the other groups. Additionally, the composite coating was biosafe and inhibited osteoclast differentiation and activity with a low attrition rate during implantation, indicating strong binding to the metal substrate. Gene set enrichment analysis showed enrichment in pathways related to Ca channel regulation, hormone binding, and signaling, suggesting the role of H-Si in promoting osteogenesis. Furthermore, a Venn plot identified 90 upregulated mRNAs associated exclusively with H-Si, with hub mRNAs, such as ADAD1 and AQP2, potentially influencing autophagy-related osteogenesis.

Cartilage tissue engineering. The use of G-based materials in tissue engineering is increasing because of their potential as culture substrates for SC and chondrocyte differentiation, in addition to their capacity to activate biomolecules and support chondrogenic differentiation and growth *via* chemical bonding (Table 2).[99] Lee *et al.* introduced G-BMSC biocomposites to induce chondrogenic differentiation *in vitro*.[100] Compared to pristine G and GO, pGO displayed a superior long-term viability, which was attributed to its porosity. Additionally, composites containing 25 μg of G and pGO exhibited optimal chondrogenic differentiation. Conversely, higher concentrations led to limitations in differentiation due to decreased cell communication and nutrient exchange, with pGO enhancing differentiation at higher concentrations due to its porous structure. Gene expression analysis corroborated these findings, indicating enhanced chondrogenesis (Col-2, SOX9, and aggrecan (ACAN)) in the pGO and GO composites. Meanwhile, cartilage tissue is required to provide structural support and enable smooth joint motion, and crucial issues in fabricating cartilage tissue engineering scaffolds include biomechanical compatibility, cell integration, and the promotion of chondrogenesis.[101] Zho *et al.* introduced a cartilage printing bioink containing GelMA, polyethylene glycol diacrylate, and GO.[102] The GO-incorporated scaffolds exhibited significantly higher protein adsorption capacity, promoting cell adhesion and growth. Furthermore, a three-wk chondrogenic differentiation study revealed that GO incorporation led to the increased synthesis of the ECM, including glycosaminoglycans (GAGs) and Col-2, which are crucial in cartilage formation. rt-qPCR analysis showed a significantly higher expression of chondrogenic markers, including Col-2, SOX9, and ACAN, within the

Table 2 G, MXene, and Xene-based tissue engineering approaches for use in cartilage regeneration

Applications	Xene materials	Formulations	Test species	Biocompatibility and therapeutic applications	Enhanced chondrogenic markers	Outlooks	Ref.
Cartilage	G and pGO	G-BMSCs biocomposite	BMSCs	50 μg mL^{-1} G and pGO did not induce cytotoxicity while 25 μg mL^{-1} GO induced long-term toxicity	Col2, Alcian blue, Sox9, and ACAN	Construction of cartilage tissues optimizing G concentrations and porosity	100
	GO	GelMA-PEGDA-GO hydrogel	BMSCs	0.25 mg mL^{-1} GO induced high cell spreading and proliferation	Alcian blue stain Col2, GAG, SOX9, ACAN	Chondrogenic differentiation with abundant ECM production for cartilage regeneration	102
		ACG/GO scaffold	hADMSCs	1 mg mL^{-1} GO enhanced cell viability and proliferation	ACAN, SOX9, Col2	Bioconjugated nanocomposite bioink showcasing excellent printability, cytocompatibility, and chondroinductive capability	104
		GO-ACM hydrogel	Rabbit BMSCs	2 mg mL^{-1} GO promoted cell adhesion and proliferation	Alcian blue, Safranin O, Col2, GAG, ACAN, SOX9	3D acellular cartilage scaffold promising treatment of articular cartilage injuries	106
			SD rats New Zealand white rabbits	Suppressed macrophage activation *in vivo*	Col1, Col2, toluidine blue, and Safranin O *in vivo*		
	$Ti_3C_2T_x$ MXene	CFOM/PLLA scaffold	Mouse BMSCs	NIR-irradiated localized hyperthermia of MXene exhibited antibacterial effects on *P. Aeruginosa* and *S. Aureus*	Alcian blue stain	NIR-triggered antimicrobial properties with photothermal and photodynamic effects for clinical treatment of tracheal injuries	107
				MXene did not hinder cell viability and proliferation	ACAN, Col2, SOX9		

GO-incorporated scaffolds, indicating the enhanced chondrogenic differentiation of the SCs. These findings suggest that GO incorporation improves protein affinity and fosters a favorable environment for chondrogenic differentiation, rendering GO a promising material for use in tissue engineering. Alg, which is a marine-derived biomaterial comprising guluronic acid and mannuronic acid, is a biocompatible, cost-effective, hydrogel-forming material frequently utilized in designing bioinks for use in 3D bioprinting, offering versatility in tissue engineering.[103] Olate-Moya *et al.* synthesized a composite bioink comprising Alg, chitosan (CS), and gel (ACG) reinforced with GO (ACG/GO) (Fig. 3).[104] GO significantly improved the proliferation, distribution, and viability of human adipose-derived mesenchymal SCs (hADMSCs) on the scaffolds. The study also assessed the chondrogenic differentiation of hADMSCs *via* the immunofluorescence staining of chondrogenic markers and detected upregulated expression of Col-2, ACAN, and SOX9, indicating the successful induction of chondrogenic differentiation. Notably, the ACG/GO scaffold with a low GO concentration (0.1 mg mL^{-1}) promoted a homogeneous cell distribution and ECM deposition, whereas the one without GO and with a high GO concentration (1 mg mL^{-1}) exhibited high-density cell aggregates. Hence, the presence of GO at low concentrations enhanced long-term cell distribution and ECM formation on the 3D printed scaffold. Meanwhile, a decellularized ECM is a preferred scaffold material because it may replicate the complex composition and topology of a natural ECM, which is distinct for each tissue, due to the intricate interactions between the resident cells and their microenvironments.[105] Gong *et al.* synthesized a GO-modified 3D acellular cartilage ECM (GO-ACM) as a printable bioink for use in cartilage tissue engineering.[106] *In vitro* chondrogenesis studies with BMSCs showed that the GO-ACM scaffolds supported cell growth and ECM production, with higher deoxyribonucleic acid and GAG contents, indicating BMSC differentiation to chondrocytes and ECM synthesis. Upon subcutaneous implantation in rats, the GO-ACM scaffolds exhibited good biocompatibility, with mild levels of inflammation at 1 wk post-surgery, which improved by wk 2, with milder inflammatory responses. In the rabbit cartilage defect model, the GO-ACM group exhibited partial scaffold degradation without significant tissue repair at 6 wk post-implantation. At 12 wk post-implantation, the GO-ACM scaffold displayed complete tissue repair with a smooth surface and mature hyaline cartilage, indicating its superior cartilage regeneration potential following *in vitro* chondrogenic induction.

To date, despite the significant potential of Xene materials in the field of cartilage tissue engineering, only a single relevant study has been presented. Qian *et al.* developed an NIR-triggered antimicrobial $CuFe_2O_4$-MXene heterojunction *via* the formation of $CuFe_2O_4$ on a Ti_3C_2 MXene, which was then uniformly incorporated into poly(L-lactic acid) (PLLA) and utilized in generating a tracheal scaffold (CFOM/PLLA).[107] The NIR-irradiated CFOM/PLLA tracheal scaffolds displayed powerful antibacterial performances, with respective antibacterial rates of 96.49% and 95.33% for *S. aureus* and *Pseudomonas aeruginosa*. Additionally, these scaffolds exhibited excellent antibiofilm activities and levels of disruption of bacterial membranes, consumption of glutathione, and generation of ROS, leading to bacterial death. Moreover, the CFOM/PLLA scaffolds released low concentrations of Cu and Fe ions to promote chondrogenic differentiation in BMSCs, as indicated by the increased levels of GAG deposition and the upregulated expression of chondrogenic genes, including ACAN, Col-2, and

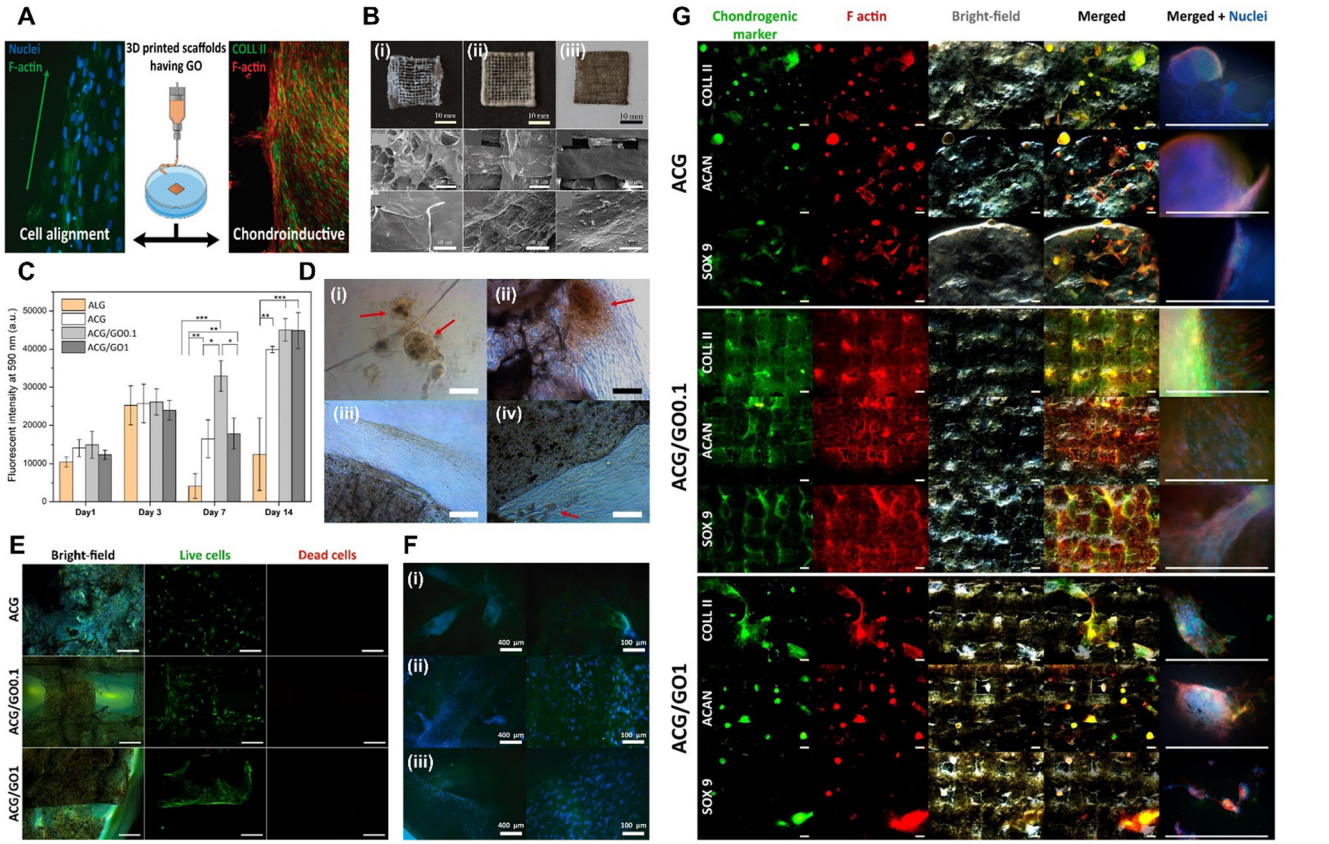

Fig. 3 Xene-based tissue engineering scaffolds for use in cartilage regeneration. (A) Schematic of the chondroinductive ACG/GO scaffold. (B) Digital and SEM images of the lyophilized 3D printed (i) ACG, (ii) ACG/GO0.1, and (iii) ACG/GO1 inks. (C) Proliferation of the hADMSCs within 14 d and (D) optical microscopy images at 7 d on (i) Alg, (ii) ACG, (iii) ACG/GO0.1, and (iv) ACG/GO1. (E) Live/dead assay of the hADMSCs seeded on each scaffold at 7 d. (F) Fluorescence microscopy images of the hADMSCs at 7 d seeded on the (i) ACG, (ii) ACG/GO0.1, and (iii) ACG/GO1 scaffolds (green: F-actin and blue: nucleus). (G) Fluorescence microscopy images of the chondrogenic markers (green), including Col-2, ACAN, and SOX9, within the 3D printed scaffolds: ACG (top), ACG/GO0.1 (middle), and ACG/GO1 (bottom), after 28 d of culture (red: F-actin and blue: nucleus). Data reproduced from ref. 104. Copyright American Chemical Society 2020. The scale bars represent 10 mm, 300 μm and 50 μm for (B) upper, middle, and lower layers, respectively; and (D) 100 μm; (E) 200 μm; (F) 400 μm (left) and 100 μm (right); and (G) 500 μm. The asterisks denote statistical significance (*$p < 0.05$, **$p < 0.01$, ***$p < 0.001$, ****$p < 0.0001$, and ns: not significant).

SOX9. Thus, the fabricated CFOM/PLLA tracheal scaffolds display potential for use in clinical applications because of their excellent antibacterial and regenerative properties.

Neuromuscular tissue engineering using G, MXenes, and Xenes

Neural tissue engineering. Despite decades of progress in understanding the biological mechanisms of the nervous system, the regeneration and repair of nerve tissues remain challenging. This is primarily because of the complex anatomy and physiology of the nervous system, which distinguishes it from other tissues, with injuries often resulting in lifelong disability.[108] However, various approaches, including auto- and allografts and pharmacological agents, have been explored, leading to increased interest in developing novel strategies, such as neural tissue engineering and nanotechnology-based approaches, for use in neural tissue regeneration (Table 3).[109] G materials exhibit hydrophilic properties and morphological characteristics that influence their capacity to interfere with neuronal and astrocyte behaviors. Small GO flakes may enhance inhibitory synapses in neuronal networks, while modifications of the O species of GO may be used to produce biocompatible substrates to promote cell adhesion, differentiation, and neurite growth (Fig. 4A–E).[110] rGO with a higher C/O ratio displays an enhanced electrical conductivity and hydrophobicity, affecting its interactions with cells and modulating biological processes, such as inflammation and neural cell differentiation.[111,112] Typically, nanofiber matrices are widely used in engineering linear tissues, such as nerves and muscles, due to their orientational guidance and capacity to endow cells with topical stimuli-responsiveness.[113] Girao *et al.* introduced size- and O group-controllable GO-laden gel and polycaprolactone (PCL) composite nanofiber matrices (rGO-PCL/gel) to induce the neurogenic differentiation of embryonic neural progenitor cells (ENMCs).[110] The rGO-PCL/gel scaffolds maintained their structural integrity and displayed distinct mechanical properties, with excellent compressive moduli. Both scaffolds promoted the formation of interconnected neural networks, with cells attaching, growing, and extending neurites

Table 3 G, MXene, and Xene-based tissue engineering approaches for use in neural tissue regeneration

Applications	Xene materials	Formulations	Test species	Biocompatibility and therapeutic applications	Enhanced neurogenic markers	Outlooks	Ref.
Neural tissues	rGO	PCL/Gel-rGO nanofiber	– Rat ENPCs	– 10 w/v% rGO enhanced cell viability	– MAP2, vimentin	Customized GO to modulate the properties of electrospun nanofibers for neural tissue engineering	110
		Ap/PLCL-rGO nanofiber	– ES, SCs, and PC12 cells – SD rats	– 2 mg mL^{-1} rGO-incorporated matrices with ES enhanced cell viability and proliferation	– NGF, PMP22, and Krox20 – Neurite length and neurogenic differentiation – *In vivo* nerve regeneration with enhanced nerve conduction velocity – Schwann cell population, myelination, and axon diameter – S100, NF200, and GFAP	Promising peripheral nerve repair and regeneration by promoting neural cell behaviors *in vitro* and facilitating nerve repair *in vivo*	114
		adECM-PLA/PCL-rGO nanofiber	– NE-4C cells – NSCs	– 1.5 wt% rGO did not hinder cell viability and proliferation	– Tuj1, GFAP, and MAP2	The adECM functionalized with PDA-rGO guiding neural stem cell adhesion, migration, and spontaneous neuronal differentiation	115
	$Ti_3C_2T_x$ MXene	MXene-PCL NGCs	– RSCs – SD rats	– 40 mg mL^{-1} MXene coating did not hinder cell viability and proliferation – No main organ damage	– Functional and histological regeneration of sciatic nerve – Gastrocnemius muscle regeneration – Myelinated axon – S100, MBP – Tuj1 and NF200 – CD34 and CD31	Promoting nerve regeneration, angiogenesis, and the transmission of physiological neural electric signals for peripheral nerve injury repair	117
		MXene-matrigel hydrogel	– SGNs – Wild-type mice	– 300 μg mL^{-1} MXene did not hinder cell growth and proliferation – EAS stimulated neural differentiation	– Neurite length with growth cone and filopodia expression – Synapsin-1, PSD95 – Calcium oscillations – NGS on neurogenic markers	Promoting neural network formation when combined with a low-frequency cochlear implant, for patients with sensorineural hearing loss through cochlear implantation	118
		MXene-PLLA nanofiber	– Mouse NSCs	– 250 μg mL^{-1} MXene NPs were cytocompatible – Anti-inflammatory reaction with less foreign body responses	– Neurite guidance with enhanced branch number, length, DCI, and intersection – Nestin, Ki67, GFAP, and Tuj1 – Synaptophysin and synaptic puncta – PI3K-Akt and Ca-signal pathway	Electrical conductivity, surface functionality, and biocompatibility, promoting NSC neurogenesis, and neurite outgrowth, making it a promising substrate for NSC engineering	119
		Lam-MXene film	– Mouse NSCs	– MXene-coating did not hinder cell viability, proliferation, and membrane integrity	– Nestin and Tuj1 – Neuronal differentiation, neurite length, branches, and dendrite protrusion – Synapsin-1, PSD95	Interface for regulating NSCs with electrically conductive interface for biosystems and future clinical applications	120
	BP	PLCL/Lam/BP nanofiber	– HT22 cell	– Cell viability was decreased at ≥ 62.5 μg mL^{-1} – 0.4 g BP-laden matrices enhanced cell proliferation	– Neurofilament heavy polypeptide – Neurite length and guidance – DCX, NeuN, MAP2, and Nestin	Neuritogenesis in hippocampal neurons for potential neural tissue engineering and regeneration	122

Table 3 (*continued*)

Applications	Xene materials	Formulations	Test species	Biocompatibility and therapeutic applications	Enhanced neurogenic markers	Outlooks	Ref.
		GelMA-BP@PDA nanofiber	– Rat BMSCs – SD rats	– 0.3 mg mL^{-1} BP@PDA with ES did not induce cytotoxicity – Cell spreading and proliferation were enhanced – ES supported neurogenic differentiation	– Nestin, Tuj1, GFAP, and MAP2	Electrical conductivity and neural differentiation of MSCs offering potential applications in tissue engineering for electroactive tissues	123
		E@BP hydrogel	– Rat primary neuron – SCI rats	– 100 μg mL^{-1} BP alleviated inflammatory effects, reduced apoptosis, and promoted proliferation – 100 μg mL^{-1} BP showed no toxicity on blood and main organs	– BBB score – CSPG, NeuN, MAP2, and GFAP – Spinal cord tissue regeneration – PDK1/AKT/GSK3 and PDK1/AKT/14-3-3/BAD pathways	Spinal cord injury repair by reducing inflammation and promoting neuronal regeneration through the activation of the AKT signaling pathway	124

along the fibrous porous structures. The scaffolds resulted in good cell viability, with minimal areas covered by dead cells, indicating no significant release of toxic products. Furthermore, rGO-PCL/gel supported the differentiation of ENMCs with neural branching and the upregulation of microtubule-associated protein 2 (MAP2) and vimentin. Wang *et al.* utilized *Antheraea pernyi*-derived silk fibroin (ApF) to enhance the cell–matrix interactions of the rGO-laden PLCL nanofiber matrices (Ap/PLCL-rGO) for use in peripheral nerve regeneration.[114] The use of Ap/PLCL-rGO, particularly when subjected to ES, led to increased gene expression of neurotrophic factors, including nerve growth factor, peripheral myelin protein 22, and early growth response 2 (Krox20), which are associated with Schwann cell myelination. Simultaneously, the expression of the neural cell adhesion molecule, which is a marker of immature SCs, was decreased. The use of Schwann cell-conditioned media cultured on Ap/PLCL-rGO with ES significantly enhanced PC12 cell differentiation with neurite outgrowth, which was attributed to the neurotrophins secreted by the Schwann cells. Subsequently, nerve guidance conduits (NGCs) were transplanted for peripheral nerve regeneration in a 10 mm sciatic nerve defect rat model, bridging the nerve defects with no signs of inflammation. Tissue weight analysis, Masson's trichrome staining, and electrophysiological studies indicated that functional recovery improved nerve conduction. Immunohistochemical and -fluorescence analyses of the regenerated nerve tissue revealed an increased Schwann cell density, myelin thickness, and axon diameter, along with increased expression of neural markers (S100 and NF200) and reduced expression of glial fibrillary acidic protein (GFAP), which is a glial marker. Meanwhile, da Silva *et al.* used adipose tissue-derived ECM (adECM) and rGO-reinforced PLA/PCL nanofiber matrices (adECM-PLA/PCL-rGO) to differentiate NE-4C neuronal cells and neural SCs (NSCs).[115] The adECM-PLA/PCL-rGO matrices provided anchoring sites for the NSCs, leading to the formation of large cell clusters, particularly in 3D constructs. The presence of rGO increased NSC metabolic activity, whereas the 3D environments with interconnected micropores promoted cell migration and spontaneous differentiation into neurons, with noticeable neurite outgrowth. Immunoblot analyses revealed significant increases in the neuronal markers Tuj1, GFAP, and MAP2a/b, indicating enhanced neuronal differentiation and neuritogenesis in the 3D adECM/PLA polydopamine (PDA)-rGO constructs.

Owing to their high electrical conductivity derived from their 2D structures and elemental nature, MXenes have also gained considerable attention in the field of neural tissue engineering.[116] Nan *et al.* developed $Ti_3C_2T_x$ MXene-coated electrospun PCL NGCs to enhance neurite regeneration and angiogenesis (Fig. 4F–L).[117] The MXene-PCL NGCs exhibited excellent biocompatibility, with no significant toxicity toward Schwann cells, good levels of cell attachment, and no abnormalities in major organs when postoperatively evaluated in rats at wk 12. The NGCs remained structurally intact but displayed some surface degradation, which did not affect their biocompatibility or levels of nerve regeneration. At 12 wk post-implantation, the MXene-PCL NGCs significantly enhanced

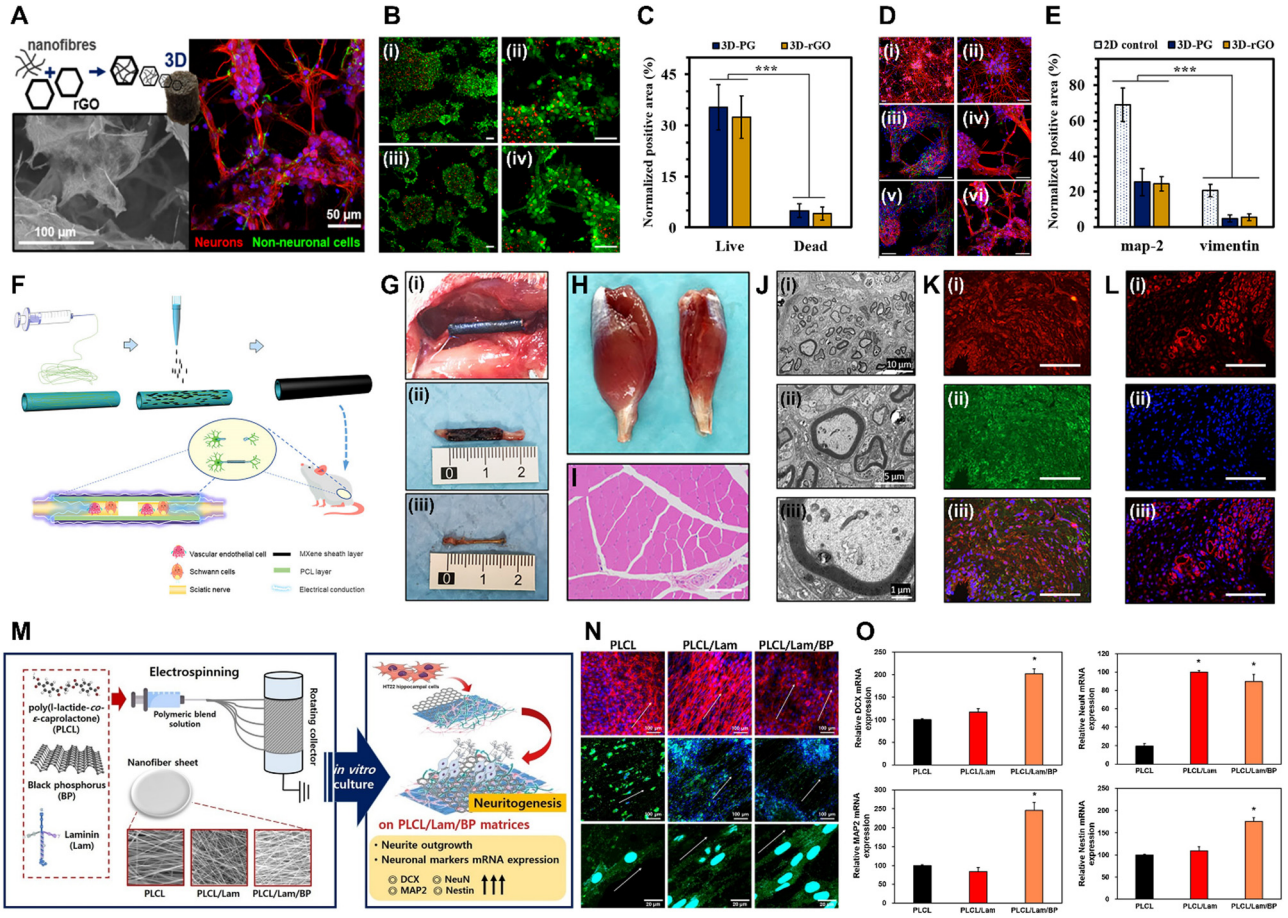

Fig. 4 Xene-based tissue engineering scaffolds for use in neural tissue regeneration. (A)–(E) PCL/Gel-rGO nanofiber scaffolds. (A) Schematic and representative fluorescence images of neurons differentiated on the PCL/Gel-rGO nanofiber scaffolds. (B) Live/dead assay and (C) quantified results of the ENMCs cultured on (i) PCL/Gel and (ii) PCL/Gel-rGO. (D) Immunofluorescence staining and (E) quantified results of the ENMCs cultured on (i) PCL/Gel and (ii) PCL/Gel-rGO (red: MAP2, green: vimentin, and blue: cell nuclei). Data reproduced from ref. 110. Copyright American Chemical Society 2020. (F)–(L) MXene-PCL NGCs. (F) Schematic of the fabrication of MXene-PCL NGCs for use in neural regeneration. (G) Morphologies of the MXene-PCL NGCs and regenerated nerve. (i) Digital image captured at 12 wk after implantation. (ii) MXene-PCL NCGs and (iii) regenerated nerves extracted from SD rats. Representative (H) optical and (I) H&E staining images of the gastrocnemius muscle at 12 wk post-operation. (J) TEM images of the cross-sections of the nerves regenerated using the MXene-PCL conduit: (i) Low-, (ii) medium-, and (iii) high-magnification images. (K) Immunofluorescence staining of S100 (red) and MBP (green) of the MXene-PCL group. (L) Immunofluorescence staining of CD34 (red) and 4′,6-diamidino-2-phenylindole (blue) of the MXene-PCL group. Data reproduced from ref. 117. Copyright Frontiers 2022. (M)–(O) PLCL/Lam/BP nanofiber matrices for use in neural tissue engineering. (M) Schematic of the electrospinning of the PLCL/Lam/BP matrices and the enhanced neuritogenesis of the HT22 cells. (N) Immunofluorescence staining of the HT22 cells cultured within each matrix (red: F-actin, blue: nucleus, and green: neurofilament). (O) Relative levels of mRNA expression of DCX, NeuN, MAP2, and nestin. Data reproduced from ref. 122. Copyright Elsevier 2020. The scale bars represent (I) and (K) 200 μm, (A-left, N and L) 100 μm, (A-right, D, B and C) 50 μm, (J-i) 10 μm, (J-ii) 5 μm, and (J-iii) 1 μm, and the asterisks denote statistical significance (*$p < 0.05$, **$p < 0.01$, ***$p < 0.001$, ****$p < 0.0001$, and ns: not significant).

gastrocnemius muscle and muscle mass restoration and increased the muscle fiber diameters. Functional recovery of the sciatic nerve, as assessed using the sciatic functional index and electrophysiological analysis, was excellent when using the MXene-PCL NGCs, and immunohistological and -fluorescence analyses revealed that these NGCs contributed to nerve fiber regeneration and myelination. Additionally, the MXene-PCL group displayed increased neovascularization, as indicated by the higher microvessel density compared to that of the PCL group, with comparable results to those of the autograft group. These findings indicate the potential of the MXene-PCL NGCs for use in promoting nerve regeneration and functional recovery. Meanwhile, Liao *et al.* introduced an ES setup prepared by integrating a cochlear implant with a conductive $Ti_3C_2T_x$ MXene-matrigel hydrogel, which was utilized to culture spiral ganglion neurons (SGNs) and expose them to ES delivered *via* the cochlear implant.[118] At concentrations of 40–100 μg mL^{-1}, the MXene-matrigel hydrogel promoted neurite outgrowth and induced significant increases in the growth cone areas and filopodia numbers of the SGNs. Additionally, the cochlear implant-MXene-matrigel hydrogel-electroacoustic stimulation (EAS) system enhanced the neurite development of the SGNs, resulting in longer neurites, larger growth cone areas, and increased filopodia numbers, without inducing

neurotoxicity. The system also promoted the formation of neural networks among the SGNs without affecting the expression or co-localization of synapsin 1 and postsynaptic density protein 95, indicating mature potential synapses. This system also increases the number of SGN synapses and enhances the Ca oscillations within the SGNs, potentially accelerating signal transmission and promoting neural network formation. RNA sequencing analysis revealed differential gene expression between the control and EAS groups, with genes related to ion transmembrane transport, synaptic transmission and plasticity, and cell adhesion significantly affected, suggesting that the system regulates various aspects of SGN behavior and function. Zhu *et al.* introduced $Ti_3C_2T_x$ MXene-coated PLLA nanofiber (MXene-PLLA) matrices for use in NSC applications.[119] The prepared MXene-PLLA matrices increased the mRNA expression levels of Tuj1 and GFAP in NSCs with the maturation of the NSC-derived neurons and astrocytes (*i.e.*, neurite branching, extended branching length, and increased dendritic complexity indices and synaptic densities). Furthermore, Kyoto Encyclopedia of Genes and Genomes analysis highlighted involvement in neuroactive ligand–receptor interactions and signaling pathways related to NSC self-renewal and Ca modulation. *In vivo* analysis indicated that the MXene-PLLA matrices exhibited excellent *in vivo* biocompatibility as they reduced foreign body responses, inflammation, and fibrotic scar formation, while enhancing matrix stability and slowing degradation, rendering them promising for use in nerve tissue engineering. Guo *et al.* investigated the neurogenic effects of a laminin-coated $Ti_3C_2T_x$ MXene (Lam-MXene) film using HT22 hippocampal neuronal cells.[120] The Lam-MXene film significantly enhanced the differentiation of NSCs to neurons, as indicated by an increased neuron content, extended neurite length, higher numbers of branch points and tips, and an improved expression of neurogenic markers (PSD95 and nestin). However, no discernible effect on synaptic development in the NSC-derived neurons was observed. In Ca imaging studies, the NSCs cultured on the Lam-MXene film exhibited spontaneous Ca spikes with high frequencies and synchronization. Moreover, ES supported the Lam-MXene film by enhancing NSC adhesion, distribution, terminal extension, and metabolism.

Meanwhile, BP aids the intercellular interactions and recovery of peripheral nerves due to its high electrical conductivity.[121] Kang *et al.* developed Lam- and BP-coated PLCL (PLCL/Lam/BP) nanofiber matrices to enhance the neuritogenesis of HT22 hippocampal cells (Fig. 4M–O).[122] Due to the hydrophilic nature of BP and Lam, the fabricated PLCL/Lam/BP matrices displayed enhanced hydrophilicity and decreased nanofiber diameters, which are favorable for neural cell growth. The levels of cell proliferation on 7 d were significantly increased in the PLCL/Lam/BP matrices, whereas no difference in initial cell adhesion was observed. HT22 cells cultured within the PLCL/Lam/BP matrices exhibited increased neurite length, with clear expression of neurofilament heavy chains. Based on mRNA analysis, doublecortin X (DCX), NeuN, MAP2, and nestin were significantly upregulated within the PLCL/Lam/BP matrices, indicating the neurogenic potential of the BP-incorporated nanofiber matrix. Xu *et al.* introduced a PDA-modified and BP-laden GelMA (GelMA-BP@PDA) hydrogel to promote the neural differentiation of rat BMSCs.[123] ES at 100 mV cm^{-1} was applied to mesenchymal SCs seeded on the GelMA-BP@PDA hydrogels, resulting in increased expression of the early neural markers nestin, Tuj1, MAP2, and GFAP, suggesting that the rat BMSCs were differentiated into neurogenic lineage. Four wks after subcutaneous implantation of the GelMA-BP@PDA hydrogel into SD rats, accelerated *in vivo* degradation was observed owing to enhanced cell infiltration and the presence of biological enzymes. Additionally, histological staining confirmed the excellent cytocompatibility of the hydrogel, with cells infiltrating and surrounding it over time, suggesting that the prepared GelMA-BP@PDA hydrogel combined with ES was favorable for use in *in vitro* neural tissue engineering and *in vivo* applications. Xie *et al.* fabricated BP quantum dot containing epigallocatechin-3-gallate (E@BP) hydrogels that target the protein kinase B (Akt) signaling pathway in spinal cord injury repair.[124] E@BP significantly improved motor function recovery in SCI rats, as indicated by their higher Basso–Beattie–Bresnahan scores and improved performances in inclined plate studies. Furthermore, E@BP treatment reduced apoptosis and promoted neural regeneration in injured neurons, as indicated by the decrease in the number of caspase-3-positive and propidium iodide/annexin double-positive neurons and the improved mitochondrial morphology. Additionally, E@BP facilitation of neural regeneration was indicated by the increase in the number of 5-ethynyl-2′-deoxyuridine-positive neurons and cell cycle progression. E@BP repaired the spinal cord tissue by reducing inflammation and promoting neuronal survival. Finally, the study investigated the molecular mechanisms underlying the effects of E@BP, revealing that it regulates the phosphoinositide-dependent kinase-1 (PDK1)/Akt/glycogen synthase kinase 3 and PDK1/Akt/14-3-3/Bcl-2-associated death promoter pathways, promotes cell cycle progression, and reduces apoptosis in SCI rats.

Muscle tissue engineering. Skeletal muscles, which constitute approximately 45% of the human body, are crucial in functions such as support, motion, and metabolic regulation. Skeletal muscle tissue engineering aims to repair or replace damaged skeletal muscles *via* various fabrication techniques, with applications spanning regenerative medicine, biorobotics and -sensing, energy harvesting, and drug screening.[125] In terms of cardiac muscle tissue engineering, the primary goal is to replicate the natural 3D tissue structure comprising cardiomyocytes (CMs), capillary endothelial and vascular smooth muscle cells, fibroblasts, and macrophages to mimic the intricate intercellular and cell–matrix interactions within the heart.[126] G materials have been extensively utilized in skeletal and cardiac muscle tissue engineering in recent decades (Table 4).[127–129] Jo *et al.* developed nano-GO-incorporated polyurethane (PU) nanofiber matrices (PU-nGO), which were mechanically flexible and myogenesis-inducing, for use in skeletal muscle tissue engineering.[130,131] The PU-nGO

Table 4 G, MXene, and Xene-based tissue engineering approaches for use in muscle tissue regeneration

Applications	Xene materials	Formulations	Test species	Biocompatibility and therapeutic applications	Enhanced myogenic markers	Outlooks	Ref.
Skeletal muscle	GO	PU-nGO nanofiber	– C2C12 cells	– 8 w/w% GO promoted cell adhesion, spreading, and proliferation – Dynamic tensional stimuli facilitated myogenesis	– MHC, α-actinin, MyoG, and MyoD	Flexibility, mechanical properties, and capacity for stimulating myogenic differentiation for skeletal muscle engineering	130
		GO/GHPA hydrogel	– C2C12 cells	– 10 μg mL^{-1} GO promoted cell growth and proliferation	– MHC and aligned myotube formation – MyoD and MyoG	3D printable GO-laden bioink for customizable skeletal muscle-mimetic constructs	132
Cardiac muscle	rGO	rGO-Col scaffold	– HUVECs	– 90 μg mL^{-1} rGO enhanced viability, spreading, and proliferation	– *In vivo* host cell migration	Enhanced mechanical properties and ability to upregulate cardiac gene expression	133
			– Rat CMs	– *In vitro* and *in vivo* angiogenesis	– Cx43, Actn4, and TrpT-2 – Cardiac muscle regeneration		
	GO	GO-PEI scaffold	– HL-1 cells	– GO coating maintained good viability and adhesion	– Cx43, Nkx 2.5, and intercellular interaction	Biocompatibility and cardiac cell growth with electrical signal conduction for cardiac tissue engineering and *in vitro* cardiac tissue models	134
Skeletal muscle	$Ti_3C_2T_x$ MXene	– MXene/AuNP/GelMA hydrogel	– C2C12 cells	– 0.05 mg mL^{-1} MXene induced high cell viability and proliferation	– MHC – Myotube maturation indexes	AuNPs and MXene improved printability, conductivity, and cellular differentiation, showing potential for muscle tissue engineering applications	136
		– MXene-F127 hydrogel	– Raw264.7 cells – C2C12 cells – HUVECs – SD rats	– 80 μg mL^{-1} MXene induced high cell viability – Antioxidant and anti-inflammatory effects – Angiogenic effects	– MHC – Myotube maturation indexes – MyoD, MyoG, and MHC – *In vivo* regeneration of myofibers and capillary	Antioxidation, anti-inflammation, and angiogenesis properties for skeletal muscle repair by regulating cell niche	140
Cardiac muscle	$Ti_3C_2T_x$ MXene	– MXene-PEG hydrogel	– iCMs	– High viability and proliferation on MXene constructs	– MYH7, TNNT2, SERCA2, and GJA1 – Ca^{2+} transient kinetics – Spontaneous beating	Clinically relevant cardiac patches for myocardial infarction treatment, addressing the need for ordered structure and electroconductivity in cardiac patches	141
		– MXene-Col film	– C3H10 cells – Rat CMs – iCMs	– 60 w/w% MXene induced cell metabolic activity and proliferation – ES stimulated maturation and elongation of iCMs – Antibacterial properties on *S. aureus*	– CMs count and spreading – cTnT, sarcomeric α-actinin, and Cx43 – action potential	Conductive biohybrid platform for cardiac tissue engineering, showing improved electrical conductivity and cell growth	142

nanofibrous membrane displayed distinct myotubular structures and well-arranged actin filaments, along with increased major histocompatibility complex (MHC) expression and upregulated mRNA levels of myogenic markers (*i.e.*, myogenin (MyoG), α-actinin, and myoblast determination protein 1 (MyoD)). Therefore, the PU-nGO nanofibers promoted myogenic differentiation owing to improved cell adhesion and their capacity to mechanically stretch cells under dynamic tensional stimuli. Kang *et al.* fabricated a 3D bioprintable GO-incorporated functionalized Gel hydrogel (GO@GHPA) for use as a skeletal muscle printing bioink (Fig. 5A–H).[132] The phenol-rich GHPA hydrogel could be crosslinked using glucose oxidase and horseradish peroxide to yield a cytocompatible crosslinked hydrogel, which was then laden with cells. The use of the 3D bioprinted GO@GHPA hydrogel resulted in enhanced cell viability, distribution, and proliferation over 7 d of culture. Over a prolonged culture period, the laden C2C12 myoblasts exhibited enhanced myotube formation and MHC expression, with the upregulation of MyoD and MyoG, suggesting the myogenic potential of GO and the GO@GHPA hydrogel. Meanwhile, Norahan *et al.* introduced rGO-incorporated Col scaffolds (Col-rGO) for use in accelerating angio- and myogenesis in cardiac tissues.[133] Cytotoxicity studies using the extracts from the Col-rGO scaffolds revealed excellent cytocompatibility, indicating that the degradation products were not harmful to the cells. Scanning electron microscopy (SEM) revealed that all scaffolds supported cell attachment and proliferation. Gene expression analysis at 7 d after seeding rat neonatal CMs on the scaffolds indicated increased levels of expression of cardiac genes, such as Cx43,

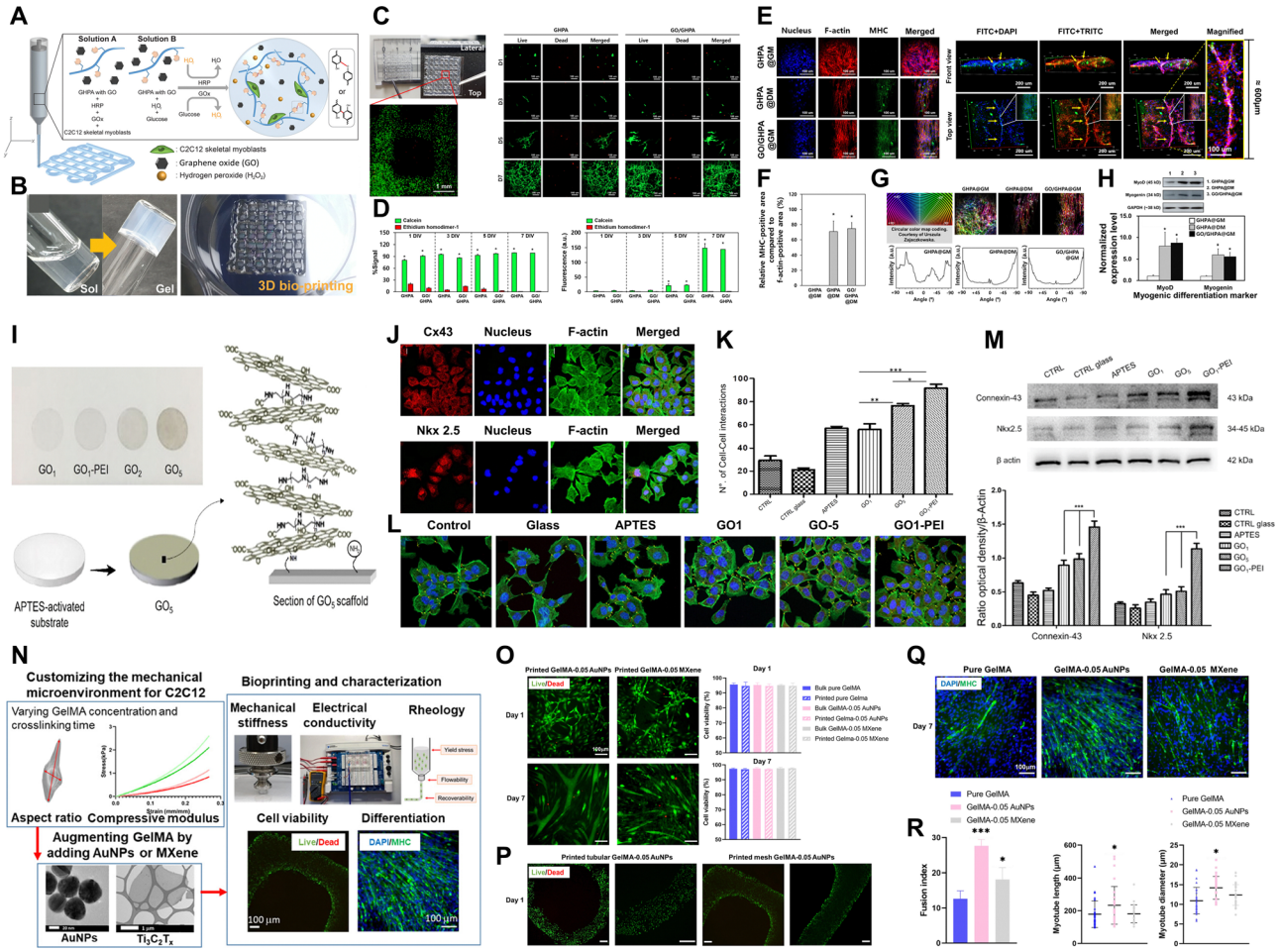

Fig. 5 Xene-based tissue engineering approaches for use in muscle tissue regeneration. (A)–(H) GO@GHPA printable bioink for use in skeletal muscle tissue regeneration. (A) Schematic of the *in situ* crosslinkable GO@GHPA hydrogel. (B) Digital images of *in situ* crosslinking and the 3D printed construct. (C) Live/dead assay within 7 d and (D) quantification. (E) Immunofluorescence staining of the C2C12 myoblasts cultured within the GO@GHPA bioinks (blue: nucleus, red: F-actin, and green: MHC). (F) Relative expression of the MHC-positive area. (G) Cell alignment quantification. (H) Relative levels of mRNA expression of the myogenic differentiation markers MyoD and MyoG. Data reproduced from ref. 132. Copyright American Chemical Society 2021. (I)–(M) GO-PEI scaffolds for use in cardiac muscle engineering. (I) Schematic of GO-PEI scaffold fabrication. (J) Immunofluorescence staining images of Cx43 (upper panel) and the expression of Nkx 2.5 (lower panel) in HL-1 cells (blue: nucleus and green: F-actin), with (K) quantification. (L) Immunofluorescence staining of Cx43 (green) in the different groups (blue: nucleus). (M) Levels of protein expression of Cx43 and Nkx 2.5 in the different groups. Data reproduced from ref. 134. Copyright American Chemical Society 2023. (N)–(R) MXene/AuNP/GelMA hydrogel for use in skeletal muscle regeneration. (N) Schematic of MXene/AuNP/GelMA hydrogel formation and characterization of the bioprinted constructs. (O) Live/dead assay and quantification of the C2C12 myoblasts cultured within the printed constructs. (P) Low-magnification results of the live/dead assays of the constructs, which were printed differently. (Q) Immunofluorescence staining of the C2C12 myoblasts cultured within the printed constructs (blue: nucleus and green: MHC). (R) Myotube maturation parameters, including fusion index and myotube length and diameter. Data reproduced from ref. 136. Copyright American Chemical Society 2021. The scale bars represent (C-left) 1 mm and (E-right) 200 μm and (C-right, E-left, N, O and Q) 100 μm, and the asterisks denote statistical significance (*$p < 0.05$, **$p < 0.01$, ***$p < 0.001$, ****$p < 0.0001$, and ns: not significant).

Actn4, and TrpT-2. *In vivo* angiogenesis was evaluated by examining subcutaneously implanted scaffolds after 2 and 4 wk, which revealed enhanced levels of cell migration and increased levels of vascularization, as indicated by enhanced capillary formation and higher rates of cell migration. Pilato *et al.* developed composite scaffolds by combining GO with polyethylenimines (PEIs) to form highly porous, biocompatible scaffolds (GO-PEI) for use in repairing damaged heart tissues following myocardial infarction and heart failure (Fig. 5I–M).[134] In cell culture studies, HL-1 cardiac muscle cells exhibited good viability and morphological stability and numerous focal adhesions and intercellular networks, indicating strong cell–substrate interactions. Moreover, the levels of expression of the cardiac markers connexin 43 (Cx43) and Nkx 2.5 were notably higher in HL-1 cells cultured on the GO-PEI substrates. This may be attributed to the hydrophilic, polycationic nature of PEI-decorated GO, which promotes cell attachment and proliferation. Additionally, the nanotopographical cues provided by the GO-PEI surfaces contributed to improved cell behaviors. Quantitative analysis further revealed a significant increase in gap junctions, indicating functional syncytia characteristic of cardiac organization, in cells cultured on GO-PEI, highlighting its

potential for use in cardiac tissue engineering. With the utilization of MXene NPs, Au NPs (AuNPs) have been widely applied in tissue engineering owing to their versatility and tunability in terms of size, morphology, surface chemistry, and other biological properties.[135] Boularaoui *et al.* introduced an AuNP- and MXene NS-laden GelMA (MXene/AuNP/GelMA) bioink for use in fabricating 3D bioprinted skeletal muscle-mimetic constructs (Fig. 5N–R).[136] The MXene/AuNP/GelMA bioinks exhibited excellent shear-thinning properties, reducing the shear stress that could harm encapsulated cells. It should be noted that GelMA crosslinking was impeded when MXene concentrations exceeded 0.1 mg mL^{-1}. The weakened crosslinking at higher MXene concentrations may be attributed to the spatial occupancy of the NPs and the interference between MXene's oxygen-containing functional groups and GelMA's amine and hydroxyl groups. This interference, in turn, hampers the free-radical photopolymerization process that GelMA undergoes when exposed to UV radiation.[137] Cell viability analysis showed no significant difference between the bulk and printed bioinks, indicating that printing did not negatively affect cell viability. Moreover, the addition of MXene and AuNPs to the bioinks enhanced skeletal muscle differentiation, as indicated by the increased fusion index and myotube length and diameter and upregulated MHC expression. Researchers attributed this improvement to the electrical conductivity of the bioinks, which may promote electrical communication between muscle cells and induce myogenic differentiation, rendering the bioinks promising for use in skeletal muscle tissue engineering. The beneficial biological properties of MXenes include free radical scavenging characteristics and anti-inflammatory activities due to M2 macrophage polarization.[138,139] Based on these properties, Ma *et al.* fabricated an MXene-laden F127 hydrogel (MXene-F127) to promote M2 macrophage polarization for skeletal muscle regeneration.[140] *In vitro* studies demonstrated that the MXene displayed strong antioxidant properties, effectively scavenged free radicals even at low concentrations, and reduced the levels of ROS in macrophages, which are induced by external stimuli. Furthermore, the MXene exhibited anti-inflammatory properties due to the downregulation of pro-inflammatory markers (*i.e.*, interleukin-1 β and tumor necrosis factor α) and promotion of the transformation of M1-type macrophages into M2-type macrophages, yielding a favorable microenvironment for myogenic differentiation and angiogenesis during skeletal muscle repair. Furthermore, the MXene enhanced the myogenic differentiation of C2C12 cells, promoting the formation of myotubes and the upregulation of myogenic genes, such as MyoD, MyoG, and MHC. The migration and angiogenesis of HUVECs were significantly promoted, facilitating the formation of complex vascular networks and the upregulation of angiogenic genes. *In vivo* studies using a rat tibialis anterior muscle defect model showed that the MXene effectively promoted skeletal muscle regeneration and the differentiation of macrophages to the M2 phenotype and reduced inflammation, further supporting its potential as a multifunctional bioactive material for use in skeletal muscle tissue regeneration. Basara *et al.* introduced 3D printed $Ti_3C_2T_x$ MXene-polyethylene glycol (MXene-PEG) composite hydrogel constructs to provide conductive and topographical cues for human induced pluripotent SC (iPSC)-derived CMs (iCMs).[141] The iCMs cultured in the MXene-PEG hydrogel exhibited improved levels of structural and sarcomere alignment and increased levels of expression of cardiac maturity-related genes (*i.e.*, MYH7, TNNT2, SERCA2, and GJA1). Electrophysiological analysis revealed that the MXene-PEG hydrogel cardiac patches exhibited spontaneous beating activities, with variations in the Ca^{2+} transient kinetics across different regions of the patterns. The conduction velocities between adjacent groups indicated synchronized beating in several regions, and detectable but slower conduction in others. Therefore, the MXene-PEG hydrogel displays potential for use in enhancing the structural and functional characteristics of iCMs in cardiac tissue engineering. A study conducted by Asaro *et al.* combined iCMs and MXene-functionalized Col (MXene-Col) films for use in cardiac tissue regeneration.[142] The MXene-Col films exhibited antibacterial properties, particularly due to the inhibition of the attachment and proliferation of *S. aureus*. These films also supported the growth of CMs and enhanced cell attachment, distribution, and maturation, which are essential in cardiac tissue engineering. When the iCMs were cultured on the MXene-Col films and exposed to an external electric field, they exhibited more mature phenotypes with improved levels of cell elongation and functional markers (*i.e.*, Cx43, cardiac troponin T, sarcomeric α-actinin, and action potential properties). These studies suggest that MXenes and ES-combined MXenes show promise for application in muscle tissue engineering.

Skin tissue engineering using G, MXenes, and Xenes

Skin tissue engineering involves preparing artificial substitutes that replicate human skin, primarily driven by the crucial role of the skin as a protective barrier against various environmental threats.[143] This field employs advanced tissue engineering techniques to develop skin substitutes for use as sophisticated models in research and in applications such as wound healing. A key challenge is the *ex vivo* expansion of cells, while preserving their normal properties, for use in transplantation or *in vitro* studies.[144] Owing to its remarkable characteristics, such as its substantial surface area-to-volume ratio, mechanical durability, antimicrobial properties, and capacity to facilitate collagen crosslinking, G is used in the field of skin tissue engineering (Table 5).[145,146]

Chu *et al.* fabricated a PEGylated, GO-mediated, quercetin (Que)-modified acellular dermal matrix (ADM; ADM-GO-PEG/Que) hybrid scaffold for use in skin tissue engineering and diabetic wound healing.[147] The GO-PEG composite displays the capacity to efficiently deliver and release various substances, including proteins, gene therapeutics, imaging agents, chemotherapy drugs, and anti-cancer medications, while enabling precise control over release.[148–150] The use of the ADM-GO-PEG/Que hybrid scaffold resulted in accelerated wound healing, with a faster rate of wound closure compared to those of other groups, reaching 87.34% closure by 21 d. Histological analysis revealed Col deposition, neovascularization, and the

Table 5 G, MXene, and Xene-based tissue engineering approaches for use in skin tissue regeneration

Applications	Xene materials	Formulations	Test species	Biocompatibility and therapeutic applications	Enhanced wound regeneration markers	Outlooks	Ref.
Skin	GO	ADM-GO-PEG/Que scaffold	– MSCs	– 50 μM GO-PEG/Que supported high cell viability, proliferation, and spreading with reduced apoptosis	– Accelerated regeneration on diabetic wounds	Improved diabetic wound healing for potential drug delivery, stem cell therapies, and tissue engineering applications	147
			– Diabetic ICR mice	– Reduced *in vivo* inflammation	– Re-epithelialization – Dermal regeneration – Collagen deposition and neovascularization – Skin appendage regeneration – Col1, Col3, and α-SMA		
	rGO	UC-GSC scaffold	– MEF cells	– Antibacterial activity against *S. aureus* and *Pseudomonas*	– *In vivo* wound closure	Efficient antibacterial properties and positive impact on cutaneous wound healing	151
			– Rat	– Support proliferation	– Re-epithelialization – Dermal regeneration – Granulation tissue and collagen fiber formation – Neovascularization		
	$Ti_3C_2T_x$ MXene	T-RMF-vitamin E nanofiber	– BMSCs	– T-RMF nanofiber matrices supported cell adhesion, spreading, and proliferation	– CD31, VEGF, and PCNA	Drug delivery and temperature-responsive wound-healing capability for future clinical applications	154
			– Kunming mice	– No toxicity on main organs – NIR-irradiated wound healing	– *In vivo* wound closure – Re-epithelialization – Dermal regeneration		
	BP	HA-DA@BP hydrogel	– GES-1 cells	– ES-supported cell behaviors and antibacterial properties	– *In vivo* wound closure	Reversible phase transformation under electrical stimulus offering promising applications in skin tissue engineering with adjustable mechanical properties, controlled drug release, and electrical antibacterial activity	155
			– Kunming mice	– Enhanced cell viability and wound healing – No hemolytic activity – No erythema or edema after transplantation – *In vitro* antibacterial property against *E. coli* – Prevention of *in vivo* bacterial inflammation	– Re-epithelialization – Dermal regeneration		
	Borophene	B-FENG nanogenerator	– L929 cells	– Enhanced cell spreading, proliferation, and *in vitro* wound healing	– *In vivo* wound closure	B-TENG with potential applications in mechanical energy harvesting, medical assistive systems, gait phase sensing, and wound monitoring and therapy, showing promise for wearable healthcare technology	157
			– SD rats	– ES support wound healing	– Re-epithelialization – Dermal regeneration		
	Stanene	Sn@PEI hydrogel	– 3T3 and L02 cells	– 150 μg mL^{-1} Sn@PEI hydrogel maintained high cell viability	– *In vivo* wound closure	Stanene treatment for drug-resistant bacterial infections and wound healing	158
			– HUVECs	– US induced antibacterial activity against *S. aureus* and MRSA	– Dermal regeneration		
			– BALB/c mice	– Hemocompatibility	– Granulation tissue with collagen deposition		
				– *In vivo* activation of inflammatory cells – ES support wound healing	– *In vivo* cell migration		
	Germanene	CS/GeNCs0.8 hydrogel	– HeLa and NIH3T3 cells	– No toxicity up to 2 mg mL^{-1}	– *In vivo* wound closure	Germanene nanocrystals for photothermal antibacterial properties and wound healing capability	161
			– Kunming mice	– NIR-irradiated antibacterial activity against *E. coli* and *S. aureus* – Hemocompatibility – No toxicity on main organs *In vivo* suppression of bacterial colony	– Re-epithelialization – Dermal regeneration		

regeneration of skin appendages, including mature vessels and hair follicles, in the ADM-GO-PEG/Que scaffold-treated group on 14 d. The ADM-GO-PEG/Que scaffold enhanced Col synthesis and capillary formation and supported the formation of granulation tissue, rendering it effective in promoting the healing of diabetic wounds. In a study conducted by Esmaeili *et al.*, nanofibrous scaffolds, denoted UC-GSC scaffolds, which were prepared using PU and cellulose acetate and contained rGO/Ag nanocomposites, were used to exploit the strong antibacterial properties of rGO/Ag.[151] The prepared UC-GSC scaffolds displayed similar rates of H_2O vapor transmission compared to those observed in other studies and biocompatibility with cells, indicating their viability for use in tissue engineering. Additionally, the scaffolds exhibited significant antibacterial activities against Gram-negative and -positive bacteria. The histological findings revealed that the UC-GSC scaffold exhibited significant improvements in wound healing, including epidermal hyperplasia, granulation tissue formation, collagen fiber deposition, and neovascularization, indicating its potential for use in promoting wound healing.

MXenes may undergo degradation *via* their interactions with H_2O and O_2, indicating that their distinctive photothermal and biodegradable attributes may be exploited practically in wound healing.[152,153] Jin *et al.* developed temperature-responsive MXene nanobelt fibers (T-RMFs) loaded with vitamin E (T-RMF-vitamin E) for use in wound healing (Fig. 6).[154] These T-RMFs exhibited photothermal properties that could be controlled using NIR irradiation, which facilitated the release of vitamin E in wound healing. The experimental results indicated that the photothermal properties of the T-RMFs were controlled under NIR irradiation, thereby ensuring safe increases in temperature. *In vitro* and *in vivo* studies confirmed the excellent biocompatibility of the T-RMFs, which promoted cell attachment and proliferation. Furthermore, the T-RMFs, which could

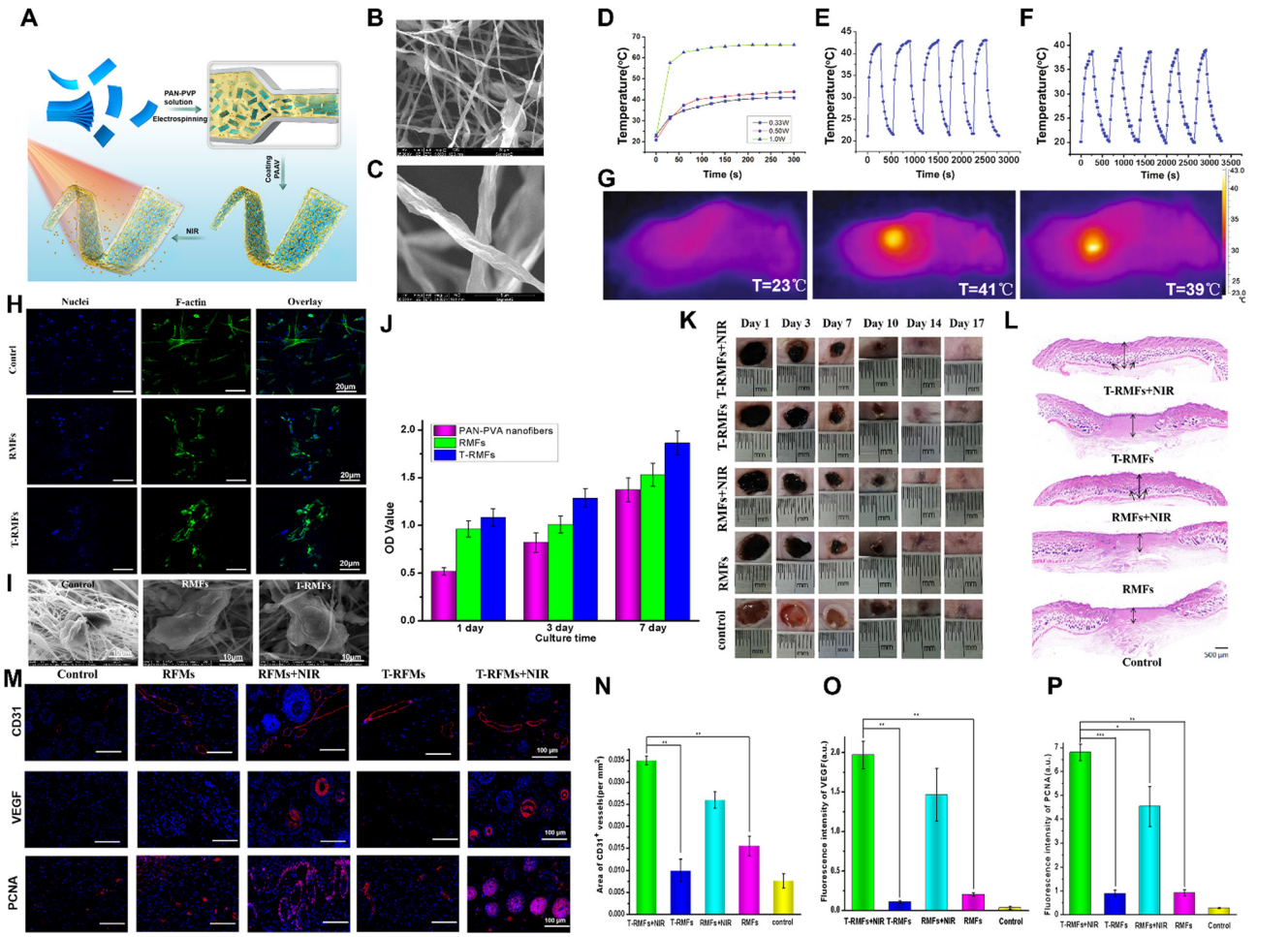

Fig. 6 Xene-based tissue engineering approaches for use in skin tissue regeneration. (A) Schematic of the fabrication of the T-RMF-vitamin E nanofiber matrices. (B) Low- and (C) high-magnification SEM images of the RMFs. (D) Heating profiles of the RMFs under 0.33, 0.50, and 1.0 W NIR light. Temperature changes of the (E) RMFs and (F) T-RMFs over 5 on/off cycles. (G) Thermal images of each group. (H) Immunofluorescence staining (blue: nucleus and green: F-actin), (I) SEM images, and (J) proliferation of the BMSCs cultured on the different nanofiber groups. (K) Representative photographs and (L) H&E staining images of the skin wounds of the various groups. (M) Immunofluorescence staining of CD31, VEGF, and PCNA of the BMSCs cultured on the different groups with or without NIR irradiation. Quantitative levels of expression of (N) CD31, (O) VEGF, and (P) PCNA. Data reproduced from ref. 154. Copyright Springer Nature 2021. The scale bars represent (M) 100 μm, (A-upper, H) 20 μm, (I) 10 μm, and (A-lower) 5 μm, and the asterisks denote statistical significance (*$p < 0.05$, **$p < 0.01$, ***$p < 0.001$, ****$p < 0.0001$, and ns: not significant).

release vitamin E under NIR exposure, significantly upregulated cluster of differentiation 31 (CD31), VEGF, and proliferating cell nuclear antigen (PCNA), which are markers of stimulated wound healing and angiogenesis. Notably, these therapeutic effects were realized with no adverse effects on the main organs, highlighting the potential of T-RMFs for use in safe, effective wound healing. BP may be utilized in skin tissue engineering by incorporating it into conductive hydrogels. Liu *et al.* prepared a conductive hydrogel, denoted HA-DA@BP, using hyaluronic acid (HA) and dopamine (DA), which was designed to produce antibacterial effects on wounds with the aid of ES.[155] The experimental results confirmed that the BP nanosheets within the hydrogel retained their original structures during degradation, and BP incorporation significantly enhanced the conductivity of the hydrogel, enabling effective electrical antibacterial activity against *Escherichia coli* when exposed to ES. Further *in vitro* studies were conducted using normal human gastric epithelial cells (GES-1), which revealed an excellent biocompatibility and the promotion of cell proliferation and migration under ES. In a mouse wound model, the HA-DA@BP hydrogel combined with ES significantly accelerated wound healing, reduced bacterial counts, and mitigated inflammation, indicating its potential for *in vivo* application as a wound dressing, with disinfection and tissue regeneration capacities.

Meanwhile, interest in borophene has been significant owing to its intricate layered structure, pronounced anisotropy, and exceptional electron transport and mechanical characteristics, but the number of studies exploring its potential in the field of tissue engineering is limited.[156] Chen *et al.* reported the utilization of a borophene/ecoflex nanocomposite-based triboelectric nanogenerator (B-TENG) in energy harvesting, medical devices, and wound healing.[157] The flexible B-TENG functioned based on triboelectricity, producing an electrical output *via* charge transfer upon contact with polyester, and it maintained its stability and durability, even after extensive evaluation and mechanical strain. The B-TENG was incorporated into a smart keyboard and robotic system for use in upper-limb medical assistance for disabled users; it was also applied in a lower-limb gait phase visualization platform to detect and display various gait phases. In terms of biological assessment, *in vitro* studies with L929 fibroblasts showed that the B-TENG could enhance cell proliferation and migration. Animal models also demonstrated the effectiveness of the B-TENG in promoting wound healing, with reduced wound sizes and improved levels of tissue regeneration. Stanene NSs (SnSNs) are semiconductors that may exhibit thickness-dependent adjustable bandgaps which render them favorable for use in cancer photothermal therapy.[63] Tao *et al.* introduced SnSNs-assembled thermosensitive poly(D,L-lactide)-PEG-poly(D,L-lactide) for use in preparing Sn@hydrogels to exploit their sonodynamic antibacterial activities.[158] Sn@PEI exhibited excellent sonodynamic properties, generating ROS effectively under ultrasound (US) irradiation, leading to antibacterial activity. Sn@PEI displayed high antibacterial efficiencies against *S. aureus* and methicillin-resistant *S. aureus* when exposed to US, whereas no significant cytotoxicity was observed toward normal cells. *In vivo* analysis revealed accelerated wound healing (full regeneration on 14 d) in mice after the transplantation of the ES-supported Sn@PEI hydrogel. The hydrogel also exhibited a potent antibacterial activity, drastically reducing the levels of bacterial contamination of infected skin wounds. Germanene displays considerable potential as a photothermal agent for use in treating infected wounds due to its efficient photothermal conversion, while its biocompatibility and low toxicity render it promising for use in clinical applications.[159,160] Therefore, Wang *et al.* developed a CS hydrogel embedded with hydroxy-functionalized germanene nanocrystals (GeNCs) *via* the crosslinking of CS and zinc acetate and self-assembly with the GeNCs to yield the photothermal wound-healing hydrogel CS/GeNCs0.8.[161] *In vitro* studies revealed that the CS/GeNCs0.8 hydrogels effectively adsorbed and killed Gram-positive *S. aureus* and Gram-negative *E. coli* when combined with NIR laser irradiation. SEM revealed that the NIR-irradiated CS/GeNCs hydrogels caused significant protein and nucleic acid leakage by disrupting membrane integrity. Additionally, the CS/GeNCs0.8 hydrogels exhibited excellent hemostatic properties and negligible hemolytic effects on red blood cells. *In vivo* studies in mice indicated that the CS/GeNCs0.8 hydrogel effectively inhibited bacterial infection and promoted wound healing, with no significant toxicity or adverse effects on body mass or the major organs, indicating its potential as a photothermal antibacterial platform for use in clinical applications.

Conclusion and future perspectives of MXene and Xene materials in tissue engineering

The achievements of G have demonstrated the feasibility of producing stable, ultra-thin layers of van der Waals materials, consisting of just one or a few atoms, using diverse techniques for fabricating single-layer, few-layer, and multi-layer assemblies in solution, on surfaces, and at a wafer scale.[162,163] In recent decades, there has been great achievement led by pioneers in the synthesis, characterization, and applications of 2D nanomaterials.[164] For instance, P. M. Ajayan led the way in the large-scale production and analysis of single layers of hexagonal boron nitride, while A. Kis and his research team achieved the synthesis of single-layer MoS_2 for use in optoelectronics and energy harvesting applications.[165,166] These advancements in 2D nanomaterials have led to increased utilization of these materials in bioengineering research, exploiting their distinctive physicochemical and biological properties.[167]

This review extensively compares the research progress of Xene-material-based tissue engineering with that of G-based materials, which have been extensively studied over the last decade. Section 2 provides an overview of the fundamental physicochemical characteristics of G, MXenes, and group III–V Xene materials. In the subsequent section, we review recent experimental advancements in Xene-based tissue engineering and regenerative medicine for different tissue types, *i.e.*, bone, cartilage, neural, muscle, and skin tissues. The versatility of

fabrication techniques (*e.g.*, 3D bioprinting and electrospinning) and cell sources (*e.g.*, SCs and primary cells) enabled researchers to produce numerous scaffolds and tissue mimetics with various structures and biofunctionalities. Each study was reviewed to explore the innovative combinations of Xene materials with other biomaterials and their capacity to promote tissue maturation from a mechanistic perspective.

The goal of tissue engineering and regenerative medicine is to prepare biomimetic constructs or matrices that provide biochemical and structural support to cells, induce the expression of intrinsic phenotypes, and facilitate differentiation to mature tissues. G-based research laid the foundation for 2D NM-based tissue engineering and serves as a valuable starting point for the subsequent development of MXene and Xene materials. Despite the promising progress, several critical challenges remain unresolved. Safety and biocompatibility are primary concerns, as the biocompatibility of most Xene materials has not been fully elucidated, necessitating further studies and long-term clinical investigations under various conditions. Understanding the interactions between Xene materials and the body (*i.e.*, biodistribution, organ accumulation, clearance pathways, inflammatory reactions, and potential genotoxicity) is crucial in exploring their future *in vivo* applications.[168] Moreover, engineered scaffolds exhibit unique complexities compared to conventional grafts, rendering the following of regulatory guidelines and processes challenging. Additionally, the multitude of active components and fabrication parameters may unpredictably affect reactions within the human body.

To address these limitations, further interdisciplinary studies and clinical trials are required to elucidate long-term efficacy and potential side effects. Standardization of culture conditions and quality control are essential to ensure the safety, efficacy, and reproducibility of Xene-based engineered scaffolds. For future clinical applications of Xene materials, it is crucial to understand the unique properties of various elemental composites and surface reactivity with the biological system in relation to their fabrication processes and structures. The ability to tailor their exterior surface functional groups enhances their adaptability for therapeutic and imaging purposes. Successful translation of preclinical findings into clinical settings, demonstrated by ongoing clinical trials, will pave the way for the acceptance and implementation of these nanomaterials in personalized medicine. Integrating nanotechnology with artificial intelligence (AI)-based methods for drug combination and dosing optimization holds great potential for enhancing the efficacy and clinical feasibility of Xene-based biomedical applications. In conclusion, researchers with diverse backgrounds should advance the field of Xene-based tissue engineering by addressing these challenges and considering the proposed suggestions.

Author contributions

Conceptualization: Moon Sung Kang, Hee Jeong Jang, Dong-Wook Han. Funding acquisition and project administration: Dong-Wook Han. Resources: Hyo Jung Jo, Iruthayapandi Selestin Raja. Supervision: Dong-Wook Han. Writing – original draft: Moon Sung Kang, Hee Jeong Jang. Writing – review & editing: Dong-Wook Han.

Conflicts of interest

There are no conflicts to declare.

Acknowledgements

This work was supported by the National Research Foundation of Korea (NRF) grant funded by the Korean Government (the Ministry of Science and ICT (MSIT)) (No. 2021R1A2C2006013), the Korea Evaluation Institute of Industrial Technology (KEIT) grant funded by the Ministry of Trade, Industry, and Energy (MOTIE, Korea) (No. 20014399), the Korea Institute for Advancement of Technology (KIAT) grant funded by the Korea Government (Ministry of Education-MOTIE) (No. P0022108, Next Generation bio-health industry Innovation Talent Training Program), and Specialization Project of Pusan National University.

References

1 S. Rahman and Y. Lu, *Nanoscale Horiz.*, 2022, **7**, 849–872.
2 K. S. Novoselov, A. K. Geim, S. V. Morozov, D.-E. Jiang, Y. Zhang, S. V. Dubonos, I. V. Grigorieva and A. A. Firsov, *Science*, 2004, **306**, 666–669.
3 O. C. Compton and S. T. Nguyen, *Small*, 2010, **6**, 711–723.
4 Y. Zhu, S. Murali, W. Cai, X. Li, J. W. Suk, J. R. Potts and R. S. Ruoff, *Adv. Mater.*, 2010, **22**, 3906–3924.
5 D. C. Marcano, D. V. Kosynkin, J. M. Berlin, A. Sinitskii, Z. Sun, A. Slesarev, L. B. Alemany, W. Lu and J. M. Tour, *ACS Nano*, 2010, **4**, 4806–4814.
6 M. K. Kumawat, M. Thakur, R. B. Gurung and R. Srivastava, *ACS Sustainable Chem. Eng.*, 2017, **5**, 1382–1391.
7 J. Shen, Y. Zhu, X. Yang and C. Li, *Chem. Commun.*, 2012, **48**, 3686–3699.
8 L. Wang, W. Li, B. Wu, Z. Li, S. Wang, Y. Liu, D. Pan and M. Wu, *Chem. Eng. J.*, 2016, **300**, 75–82.
9 M. T. Hwang, M. Heiranian, Y. Kim, S. You, J. Leem, A. Taqieddin, V. Faramarzi, Y. Jing, I. Park and A. M. van der Zande, *Nat. Commun.*, 2020, **11**, 1543.
10 Z. Gu, S. Zhu, L. Yan, F. Zhao and Y. Zhao, *Adv. Mater.*, 2019, **31**, 1800662.
11 G. Cellot, S. Vranic, Y. Shin, R. Worsley, A. F. Rodrigues, C. Bussy, C. Casiraghi, K. Kostarelos and J. R. McDearmid, *Nanoscale Horiz.*, 2020, **5**, 1250–1263.
12 X. Sun, Z. Liu, K. Welsher, J. T. Robinson, A. Goodwin, S. Zaric and H. Dai, *Nano Res.*, 2008, **1**, 203–212.
13 Y. Qian, X. Zhao, Q. Han, W. Chen, H. Li and W. Yuan, *Nat. Commun.*, 2018, **9**, 323.

14 Y.-T. Kwon, Y.-S. Kim, S. Kwon, M. Mahmood, H.-R. Lim, S.-W. Park, S.-O. Kang, J. J. Choi, R. Herbert and Y. C. Jang, *Nat. Commun.*, 2020, **11**, 3450.
15 R. D. Rodriguez, A. Khalelov, P. S. Postnikov, A. Lipovka, E. Dorozhko, I. Amin, G. V. Murastov, J.-J. Chen, W. Sheng and M. E. Trusova, *Mater. Horiz.*, 2020, **7**, 1030–1041.
16 W. Shao, L. Zhang, Z. Jiang, M. Xu, Y. Chen, S. Li and C. Liu, *Nanoscale Horiz.*, 2022, **7**, 1411–1417.
17 K. Tadyszak, J. K. Wychowaniec and J. Litowczenko, *Nanomaterials*, 2018, **8**, 944.
18 S. R. Shin, B. Aghaei-Ghareh-Bolagh, T. T. Dang, S. N. Topkaya, X. Gao, S. Y. Yang, S. M. Jung, J. H. Oh, M. R. Dokmeci and X. Tang, *Adv. Mater.*, 2013, **25**, 6385–6391.
19 N. Dubey, R. Bentini, I. Islam, T. Cao, A. H. Castro Neto and V. Rosa, *Stem Cells Int.*, 2015, **2015**, 804213.
20 T. Hu, X. Mei, Y. Wang, X. Weng, R. Liang and M. Wei, *Sci. Bull.*, 2019, **64**, 1707–1727.
21 M. Naguib, M. Kurtoglu, V. Presser, J. Lu, J. Niu, M. Heon, L. Hultman, Y. Gogotsi and M. W. Barsoum, *Adv. Mater.*, 2011, **23**, 4248–4253.
22 S. Pan, J. Yin, L. Yu, C. Zhang, Y. Zhu, Y. Gao and Y. Chen, *Adv. Sci.*, 2020, **7**, 1901511.
23 H. Lin, S. Gao, C. Dai, Y. Chen and J. Shi, *J. Am. Chem. Soc.*, 2017, **139**, 16235–16247.
24 S. Iravani and R. S. Varma, *Mater. Adv.*, 2021, **2**, 2906–2917.
25 Y. Zhong, S. Huang, Z. Feng, Y. Fu and A. Mo, *J. Biomed. Mater. Res., Part A*, 2022, **110**, 1840–1859.
26 R. Huang, X. Chen, Y. Dong, X. Zhang, Y. Wei, Z. Yang, W. Li, Y. Guo, J. Liu and Z. Yang, *ACS Appl. Bio Mater.*, 2020, **3**, 2125–2131.
27 R. Yang, S. Wen, S. Cai, W. Zhang, T. Wu and Y. Xiong, *Nanoscale Horiz.*, 2023, **8**(10), 1333–1344.
28 H. Qiao, H. Liu, Z. Huang, R. Hu, Q. Ma, J. Zhong and X. Qi, *Energy Environ. Mater.*, 2021, **4**, 522–543.
29 W. Tao, N. Kong, X. Ji, Y. Zhang, A. Sharma, J. Ouyang, B. Qi, J. Wang, N. Xie and C. Kang, *Chem. Soc. Rev.*, 2019, **48**, 2891–2912.
30 W. Tao, X. Ji, X. Zhu, L. Li, J. Wang, Y. Zhang, P. E. Saw, W. Li, N. Kong and M. A. Islam, *Adv. Mater.*, 2018, **30**, 1802061.
31 M. Qiu, A. Singh, D. Wang, J. Qu, M. Swihart, H. Zhang and P. N. Prasad, *Nano Today*, 2019, **25**, 135–155.
32 H. Huang, W. Feng and Y. Chen, *Chem. Soc. Rev.*, 2021, **50**, 11381–11485.
33 S. Zhu, Y. Liu, Z. Gu and Y. Zhao, *Adv. Drug Delivery Rev.*, 2022, 114420.
34 M. C. Shin, M. S. Kang, R. Park, S. Y. Chae, D.-W. Han and S. W. Hong, *Appl. Surf. Sci.*, 2021, **561**, 150115.
35 B. Konkena and S. Vasudevan, *J. Phys. Chem. Lett.*, 2012, **3**, 867–872.
36 L. Sun, *Chin. J. Chem. Eng.*, 2019, **27**, 2251–2260.
37 D. Chimene, D. L. Alge and A. K. Gaharwar, *Adv. Mater.*, 2015, **27**, 7261–7284.
38 R. Tarcan, O. Todor-Boer, I. Petrovai, C. Leordean, S. Astilean and I. Botiz, *J. Mater. Chem. C*, 2020, **8**, 1198–1224.
39 Y. Shen, S. Yang, P. Zhou, Q. Sun, P. Wang, L. Wan, J. Li, L. Chen, X. Wang and S. Ding, *Carbon*, 2013, **62**, 157–164.
40 Y. Guan, S. Jiang, Y. Cong, J. Wang, Z. Dong, Q. Zhang, G. Yuan, Y. Li and X. Li, *2D Mater.*, 2020, **7**, 025010.
41 B. Zazoum, *Mater. Sci. Forum*, 2022, **1053**, 77–82.
42 Q. Zhong, Y. Li and G. Zhang, *Chem. Eng. J.*, 2021, **409**, 128099.
43 X. Li, X. Yin, S. Liang, M. Li, L. Cheng and L. Zhang, *Carbon*, 2019, **146**, 210–217.
44 M. Soleymaniha, M. A. Shahbazi, A. R. Rafieerad, A. Maleki and A. Amiri, *Adv. Healthcare Mater.*, 2019, **8**, 1801137.
45 Q. Guo, K. Wu, Z. Shao, E. T. Basore, P. Jiang and J. Qiu, *Adv. Opt. Mater.*, 2019, **7**, 1900322.
46 H. Braunschweig, P. Constantinidis, T. Dellermann, W. C. Ewing, I. Fischer, M. Hess, F. R. Knight, A. Rempel, C. Schneider and S. Ullrich, *Angew. Chem., Int. Ed.*, 2016, **55**, 5606–5609.
47 A. R. Oganov, J. Chen, C. Gatti, Y. Ma, Y. Ma, C. W. Glass, Z. Liu, T. Yu, O. O. Kurakevych and V. L. Solozhenko, *Nature*, 2009, **457**, 863–867.
48 S. Qi, J. Liu, Y. Li and M. Zhao, *Phys. Rev. B*, 2022, **106**, 165204.
49 N. Wächter, C. Munson, R. Jarošová, I. Berkun, T. Hogan, R. C. Rocha-Filho and G. M. Swain, *ACS Appl. Mater. Interfaces*, 2016, **8**, 28325–28337.
50 M. I. Eremets, V. V. Struzhkin, H.-K. Mao and R. J. Hemley, *Science*, 2001, **293**, 272–274.
51 A. J. Mannix, Z. Zhang, N. P. Guisinger, B. I. Yakobson and M. C. Hersam, *Nat. Nanotechnol.*, 2018, **13**, 444–450.
52 X. Ji, N. Kong, J. Wang, W. Li, Y. Xiao, S. T. Gan, Y. Zhang, Y. Li, X. Song and Q. Xiong, *Adv. Mater.*, 2018, **30**, 1803031.
53 A. Molle, C. Grazianetti, L. Tao, D. Taneja, M. H. Alam and D. Akinwande, *Chem. Soc. Rev.*, 2018, **47**, 6370–6387.
54 H. J. Zandvliet, *Nano Today*, 2014, **9**, 691–694.
55 C.-C. Liu, W. Feng and Y. Yao, *Phys. Rev. Lett.*, 2011, **107**, 076802.
56 A. J. Mannix, B. Kiraly, M. C. Hersam and N. P. Guisinger, *Nat. Rev. Chem.*, 2017, **1**, 0014.
57 H. Lin, W. Qiu, J. Liu, L. Yu, S. Gao, H. Yao, Y. Chen and J. Shi, *Adv. Mater.*, 2019, **31**, 1903013.
58 A. Acun, L. Zhang, P. Bampoulis, M. V. Farmanbar, A. van Houselt, A. Rudenko, M. Lingenfelder, G. Brocks, B. Poelsema and M. Katsnelson, *J. Phys.: Condens. Matter*, 2015, **27**, 443002.
59 C. Si, J. Liu, Y. Xu, J. Wu, B.-L. Gu and W. Duan, *Phys. Rev. B: Condens. Matter Mater. Phys.*, 2014, **89**, 115429.
60 S. Noreen, M. B. Tahir, A. Hussain, T. Nawaz, J. U. Rehman, A. Dahshan, M. Alzaid and H. Alrobei, *Int. J. Hydrogen Energy*, 2022, **47**, 1371–1389.
61 Y. Shaidu and O. Akin-Ojo, *Comput. Mater. Sci.*, 2016, **118**, 11–15.
62 P. Garg, I. Choudhuri, A. Mahata and B. Pathak, *Phys. Chem. Chem. Phys.*, 2017, **19**, 3660–3669.
63 J. Ouyang, L. Zhang, L. Li, W. Chen, Z. Tang, X. Ji, C. Feng, N. Tao, N. Kong and T. Chen, *Nano-Micro Lett.*, 2021, **13**, 1–18.

64 S. Zhang, S. Guo, Z. Chen, Y. Wang, H. Gao, J. Gómez-Herrero, P. Ares, F. Zamora, Z. Zhu and H. Zeng, *Chem. Soc. Rev.*, 2018, **47**, 982–1021.
65 M. Sun, W. Tang, Q. Ren, S.-K. Wang, J. Yu and Y. Du, *Appl. Surf. Sci.*, 2015, **356**, 110–114.
66 X. Yu, W. Liang, C. Xing, K. Chen, J. Chen, W. Huang, N. Xie, M. Qiu, X. Yan and Z. Xie, *J. Mater. Chem. A*, 2020, **8**, 12887–12927.
67 W. Lu, H. Nan, J. Hong, Y. Chen, C. Zhu, Z. Liang, X. Ma, Z. Ni, C. Jin and Z. Zhang, *Nano Res.*, 2014, **7**, 853–859.
68 V. Sresht, A. A. Padua and D. Blankschtein, *ACS Nano*, 2015, **9**, 8255–8268.
69 S. Lee, Y. Lee, L. P. Ding, K. Lee, F. Ding and K. Kim, *ACS Nano*, 2022, **16**, 12822–12830.
70 L. Qiu, J. Dong and F. Ding, *Nanoscale*, 2018, **10**, 2255–2259.
71 M. Zhang, G. M. Biesold and Z. Lin, *Chem. Soc. Rev.*, 2021, **50**, 13346–13371.
72 M. Batmunkh, M. Bat-Erdene and J. G. Shapter, *Adv. Mater.*, 2016, **28**, 8586–8617.
73 M. S. Kang, R. Park, H. J. Jo, Y. C. Shin, C.-S. Kim, S.-H. Hyon, S. W. Hong, J. Oh and D.-W. Han, *Cells*, 2023, **12**, 1448.
74 Y. C. Shin, J.-H. Bae, J. H. Lee, I. S. Raja, M. S. Kang, B. Kim, S. W. Hong, J.-B. Huh and D.-W. Han, *Biomater. Res.*, 2022, **26**, 11.
75 X. Wu, X. Liu, J. Wang, J. Huang and S. Yang, *ACS Appl. Mater. Interfaces*, 2018, **10**, 39009–39017.
76 M. S. Kang, S. J. Jeong, S. H. Lee, B. Kim, S. W. Hong, J. H. Lee and D.-W. Han, *Biomater. Res.*, 2021, **25**, 1–9.
77 M. S. Kang, J. Jang, H. J. Jo, W.-H. Kim, B. Kim, H.-J. Chun, D. Lim and D.-W. Han, *Biomolecules*, 2022, **13**, 55.
78 Q.-C. Tan, X.-S. Jiang, L. Chen, J.-F. Huang, Q.-X. Zhou, J. Wang, Y. Zhao, B. Zhang, Y.-N. Sun and M. Wei, *Mater. Today Bio*, 2023, **18**, 100500.
79 J. Yin, S. Pan, X. Guo, Y. Gao, D. Zhu, Q. Yang, J. Gao, C. Zhang and Y. Chen, *Nano-Micro Lett.*, 2021, **13**, 1–18.
80 J. Zhang, Y. Fu and A. Mo, *Int. J. Nanomed.*, 2019, 10091–10103.
81 Z.-C. Hu, J.-Q. Lu, T.-W. Zhang, H.-F. Liang, H. Yuan, D.-H. Su, W. Ding, R.-X. Lian, Y.-X. Ge and B. Liang, *Bioact. Mater.*, 2023, **22**, 1–17.
82 T. F. Cabada, M. Ruben, A. El Merhie, R. P. Zaccaria, A. Alabastri, E. M. Petrini, A. Barberis, M. Salerno, M. Crepaldi and A. Davis, *Nanoscale Horiz.*, 2023, **8**, 95–107.
83 P. Bhattacharjee, B. Kundu, D. Naskar, H.-W. Kim, T. K. Maiti, D. Bhattacharya and S. C. Kundu, *Acta Biomater.*, 2017, **63**, 1–17.
84 K. Soetan, C. Olaiya and O. Oyewole, *Afr. J. Food Sci.*, 2010, **4**, 200–222.
85 X. Liu, M. N. George, L. Li, D. Gamble, A. L. Miller II, B. Gaihre, B. E. Waletzki and L. Lu, *ACS Biomater. Sci. Eng.*, 2020, **6**, 4653–4665.
86 K. Huang, J. Wu and Z. Gu, *ACS Appl. Mater. Interfaces*, 2018, **11**, 2908–2916.
87 Y. Miao, X. Shi, Q. Li, L. Hao, L. Liu, X. Liu, Y. Chen and Y. Wang, *Biomater. Sci.*, 2019, **7**, 4046–4059.
88 T. Xin, Y. Gu, R. Cheng, J. Tang, Z. Sun, W. Cui and L. Chen, *ACS Appl. Mater. Interfaces*, 2017, **9**, 41168–41180.
89 E. R. Janeček, J. R. McKee, C. S. Tan, A. Nykänen, M. Kettunen, J. Laine, O. Ikkala and O. A. Scherman, *Angew. Chem., Int. Ed.*, 2015, **54**, 5383–5388.
90 C. T. Price, K. J. Koval and J. R. Langford, *Int. J. Endocrinol.*, 2013, **2013**, 316783.
91 F. Wang, H. Duan, R. Zhang, H. Guo, H. Lin and Y. Chen, *Nanoscale*, 2020, **12**, 17931–17946.
92 C. He, L. Yu, L. Ding, H. Yao, Y. Chen and Y. Hao, *Biomaterials*, 2020, **255**, 120181.
93 N. Ni, M. Ge, R. Huang, D. Zhang, H. Lin, Y. Ju, Z. Tang, H. Gao, H. Zhou and Y. Chen, *Adv. Healthcare Mater.*, 2023, **12**, 2203107.
94 Z. Lin, Z. Chen, Y. Chen, N. Yang, J. Shi, Z. Tang, C. Zhang, H. Lin and J. Yin, *Exploration*, 2023, **3**, 20220149.
95 H. Zhou and J. Lee, *Acta Biomater.*, 2011, **7**, 2769–2781.
96 B. Yuan, M. Xue, Y. Zhao, Q. Guo, G. Zheng, Z. Xu, F. Li, X. Chen, Z. Chen and J. Shi, *Nano Today*, 2023, **52**, 101959.
97 J. Zhang, H. Eyisoylu, X.-H. Qin, M. Rubert and R. Müller, *Acta Biomater.*, 2021, **121**, 637–652.
98 H. J. Jang, M. S. Kang, W.-H. Kim, H. J. Jo, S.-H. Lee, E. J. Hahm, J. H. Oh, S. W. Hong, B. Kim and D.-W. Han, *Nanoscale Adv.*, 2023, **5**(14), 3619–3628.
99 N. Amiryaghoubi, M. Fathi, J. Barar, N. Noroozi-Pesyan, H. Omidian and Y. Omidi, *J. Drug Delivery Sci. Technol.*, 2023, 104437.
100 W. C. Lee, C. H. Lim, Kenry, C. Su, K. P. Loh and C. T. Lim, *Small*, 2015, **11**, 963–969.
101 Y. Liu, G. Zhou and Y. Cao, *Engineering*, 2017, **3**, 28–35.
102 X. Zhou, M. Nowicki, H. Cui, W. Zhu, X. Fang, S. Miao, S.-J. Lee, M. Keidar and L. G. Zhang, *Carbon*, 2017, **116**, 615–624.
103 E. Axpe and M. L. Oyen, *Int. J. Mol. Sci.*, 2016, **17**, 1976.
104 F. Olate-Moya, L. Arens, M. Wilhelm, M. A. Mateos-Timoneda, E. Engel and H. Palza, *ACS Appl. Mater. Interfaces*, 2020, **12**, 4343–4357.
105 F. Pati, J. Jang, D.-H. Ha, S. Won Kim, J.-W. Rhie, J.-H. Shim, D.-H. Kim and D.-W. Cho, *Nat. Commun.*, 2014, **5**, 3935.
106 M. Gong, J. Sun, G. Liu, L. Li, S. Wu and Z. Xiang, *Mater. Sci. Eng., C*, 2021, **119**, 111603.
107 G. Qian, L. Zhang, Y. Shuai, X. Wu, Z. Zeng, S. Peng and C. Shuai, *Appl. Surf. Sci.*, 2023, **614**, 156108.
108 A. Halim, K.-Y. Qu, X.-F. Zhang and N.-P. Huang, *ACS Biomater. Sci. Eng.*, 2021, **7**, 3503–3529.
109 P. Gupta, P. Rathi, R. Gupta, H. Baldi, Q. Coquerel, A. Debnath, H. G. Derami, B. Raman and S. Singamaneni, *Nanoscale Horiz.*, 2023, **8**(11), 1537–1555.
110 A. F. Girao, J. Sousa, A. Dominguez-Bajo, A. Gonzalez-Mayorga, I. Bdikin, E. Pujades-Otero, N. Casan-Pastor, M. J. Hortigüela, G. Otero-Irurueta and A. Completo, *ACS Appl. Mater. Interfaces*, 2020, **12**, 38962–38975.

111 S. A. Sydlik, S. Jhunjhunwala, M. J. Webber, D. G. Anderson and R. Langer, *ACS Nano*, 2015, **9**, 3866–3874.
112 O. Akhavan, E. Ghaderi, E. Abouei, S. Hatamie and E. Ghasemi, *Carbon*, 2014, **66**, 395–406.
113 X. Li, Y. Ren, Y. Xue, Y. Zhang and Y. Liu, *Nanoscale Horiz.*, 2023, **8**(10), 1313–1332.
114 J. Wang, Y. Cheng, L. Chen, T. Zhu, K. Ye, C. Jia, H. Wang, M. Zhu, C. Fan and X. Mo, *Acta Biomater.*, 2019, **84**, 98–113.
115 D. M. da Silva, N. Barroca, S. C. Pinto, Â. Semitela, B. M. de Sousa, P. A. Martins, L. Nero, I. Madarieta, N. García-Urkia and F.-J. Fernández-San-Argimiro, *Chem. Eng. J.*, 2023, **472**, 144980.
116 C. Qiao, H. Wu, X. Xu, Z. Guan and W. Ou-Yang, *Adv. Mater. Interfaces*, 2021, **8**, 2100903.
117 L.-P. Nan, Z. Lin, F. Wang, X.-H. Jin, J.-Q. Fang, B. Xu, S.-H. Liu, F. Zhang, Z. Wu and Z.-F. Zhou, *Front. Bioeng. Biotechnol.*, 2022, **10**, 850650.
118 M. Liao, Y. Hu, Y. Zhang, K. Wang, Q. Fang, Y. Qi, Y. Shen, H. Cheng, X. Fu and M. Tang, *ACS Nano*, 2022, **16**, 16744–16756.
119 Y. D. Zhu, X. Y. Ma, L. P. Li, Q. J. Yang, F. Jin, Z. N. Chen, C. P. Wu, H. B. Shi, Z. Q. Feng and S. K. Yin, *Adv. Healthcare Mater.*, 2023, 2300731.
120 R. Guo, M. Xiao, W. Zhao, S. Zhou, Y. Hu, M. Liao, S. Wang, X. Yang, R. Chai and M. Tang, *Acta Biomater.*, 2022, **139**, 105–117.
121 Y. Qian, W.-E. Yuan, Y. Cheng, Y. Yang, X. Qu and C. Fan, *Nano Lett.*, 2019, **19**, 8990–9001.
122 M. S. Kang, S.-J. Song, J. H. Cha, Y. Cho, H. U. Lee, S.-H. Hyon, J. H. Lee and D.-W. Han, *J. Ind. Eng. Chem.*, 2020, **92**, 226–235.
123 C. Xu, Y. Xu, M. Yang, Y. Chang, A. Nie, Z. Liu, J. Wang and Z. Luo, *Adv. Funct. Mater.*, 2020, **30**, 2000177.
124 D.-M. Xie, C. Sun, Q. Tu, S. Li, Y. Zhang, X. Mei and Y. Li, *J. Tissue Eng.*, 2023, **14**, 20417314231180033.
125 S. Ostrovidov, S. Salehi, M. Costantini, K. Suthiwanich, M. Ebrahimi, R. B. Sadeghian, T. Fujie, X. Shi, S. Cannata and C. Gargioli, *Small*, 2019, **15**, 1805530.
126 F. Weinberger, I. Mannhardt and T. Eschenhagen, *Circ. Res.*, 2017, **120**, 1487–1500.
127 Y. C. Shin, S.-J. Song, J. H. Lee, R. Park, M. S. Kang, Y. B. Lee, S. W. Hong and D.-W. Han, *Sci. Adv. Mater.*, 2020, **12**, 474–480.
128 S. H. Kang, Y. C. Shin, E. Y. Hwang, J. H. Lee, C.-S. Kim, Z. Lin, S. H. Hur, D.-W. Han and S. W. Hong, *Mater. Horiz.*, 2019, **6**, 1066–1079.
129 Y. C. Shin, S. H. Kang, J. H. Lee, B. Kim, S. W. Hong and D.-W. Han, *J. Biomater. Sci., Polym. Ed.*, 2018, **29**, 762–774.
130 S. B. Jo, U. Erdenebileg, K. Dashnyam, G.-Z. Jin, J.-R. Cha, A. El-Fiqi, J. C. Knowles, K. D. Patel, H.-H. Lee and J.-H. Lee, *J. Tissue Eng.*, 2020, **11**, 2041731419900424.
131 Y. C. Shin, C. Kim, S.-J. Song, S. Jun, C.-S. Kim, S. W. Hong, S.-H. Hyon, D.-W. Han and J.-W. Oh, *Nanotheranostics*, 2018, **2**, 144.
132 M. S. Kang, J. I. Kang, P. Le Thi, K. M. Park, S. W. Hong, Y. S. Choi, D.-W. Han and K. D. Park, *ACS Macro Lett.*, 2021, **10**, 426–432.
133 M. H. Norahan, M. Amroon, R. Ghahremanzadeh, M. Mahmoodi and N. Baheiraei, *J. Biomed. Mater. Res., Part A*, 2019, **107**, 204–219.
134 S. Pilato, S. Moffa, G. Siani, F. Diomede, O. Trubiani, J. Pizzicannella, D. Capista, M. Passacantando, P. Samorì and A. Fontana, *ACS Appl. Mater. Interfaces*, 2023, **15**, 14077–14088.
135 B. Salesa, P. Ferrús-Manzano, A. Tuñón-Molina, A. Cano-Vicent, M. Assis, J. Andrés and Á. Serrano-Aroca, *Chem. – Biol. Interact.*, 2023, **382**, 110646.
136 S. Boularaoui, A. Shanti, M. Lanotte, S. Luo, S. Bawazir, S. Lee, N. Christoforou, K. A. Khan and C. Stefanini, *ACS Biomater. Sci. Eng.*, 2021, **7**, 5810–5822.
137 S. H. Lee, M. S. Kang, S. Jeon, H. J. Jo, S. W. Hong, B. Kim and D.-W. Han, *Heliyon*, 2023, **9**, e14490.
138 J. Liu, W. Lu, X. Lu, L. Zhang, H. Dong and Y. Li, *Nano Res.*, 2022, 1–9.
139 J. Zhang, Y. Wang, N. Ding, P. Ma, Z. Zhang and Y. Liu, *Colloids Interface Sci. Commun.*, 2023, **56**, 100733.
140 T. Li, J. Ma, W. Wang and B. Lei, *Adv. Healthcare Mater.*, 2023, **12**, 2201862.
141 G. Basara, M. Saeidi-Javash, X. Ren, G. Bahcecioglu, B. C. Wyatt, B. Anasori, Y. Zhang and P. Zorlutuna, *Acta Biomater.*, 2022, **139**, 179–189.
142 G. A. Asaro, M. Solazzo, M. Suku, D. Spurling, K. Genoud, J. G. Gonzalez, F. J. O. Brien, V. Nicolosi and M. G. Monaghan, *npj 2D Mater. Appl.*, 2023, **7**, 44.
143 Z. Han, M. Yuan, L. Liu, K. Zhang, B. Zhao, B. He, Y. Liang and F. Li, *Nanoscale Horiz.*, 2023, **8**, 422–440.
144 F. Groeber, M. Holeiter, M. Hampel, S. Hinderer and K. Schenke-Layland, *Adv. Drug Delivery Rev.*, 2011, **63**, 352–366.
145 I. S. Raja, H. J. Jang, M. S. Kang, K. S. Kim, Y. S. Choi, J.-R. Jeon, J. H. Lee and D.-W. Han, *Multifaceted Biomedical Applications of Graphene*, 2022, pp. 89–105.
146 I. S. Raja, H. J. Jang, M. S. Kang, K. S. Kim, Y. S. Choi, J.-R. Jeon, J. H. Lee and D.-W. Han, in *Advances in Experimental Medicine and Biology*, ed. D. -W. Han and S. W. Hong, Springer, Berlin, 1st edn, 2022, ch. 3, pp. 89–105.
147 J. Chu, P. Shi, W. Yan, J. Fu, Z. Yang, C. He, X. Deng and H. Liu, *Nanoscale*, 2018, **10**, 9547–9560.
148 H. Shen, M. Liu, H. He, L. Zhang, J. Huang, Y. Chong, J. Dai and Z. Zhang, *ACS Appl. Mater. Interfaces*, 2012, **4**, 6317–6323.
149 K. Yang, S. Zhang, G. Zhang, X. Sun, S.-T. Lee and Z. Liu, *Nano Lett.*, 2010, **10**, 3318–3323.
150 L. Feng, X. Yang, X. Shi, X. Tan, R. Peng, J. Wang and Z. Liu, *Small*, 2013, **9**, 1989–1997.
151 E. Esmaeili, T. Eslami-Arshaghi, S. Hosseinzadeh, E. Elahirad, Z. Jamalpoor, S. Hatamie and M. Soleimani, *Int. J. Biol. Macromol.*, 2020, **152**, 418–427.
152 X. Xu, S. Wang, H. Wu, Y. Liu, F. Xu and J. Zhao, *Colloids Surf., B*, 2021, **207**, 111979.

153 C. Liang, J. He, Y. Cao, G. Liu, C. Zhang, Z. Qi, C. Fu and Y. Hu, *J. Biol. Eng.*, 2023, **17**, 39.
154 L. Jin, X. Guo, D. Gao, C. Wu, B. Hu, G. Tan, N. Du, X. Cai, Z. Yang and X. Zhang, *NPG Asia Mater.*, 2021, **13**, 24.
155 W. Liu, Z. Tao, Y. Chen, Y. Zhu, L. Zhang and A. Dong, *Adv. Healthcare Mater.*, 2023, 2301817.
156 P. Ranjan, J. M. Lee, P. Kumar and A. Vinu, *Adv. Mater.*, 2020, **32**, 2000531.
157 S. W. Chen, S. M. Huang, H. S. Wu, W. P. Pan, S. M. Wei, C. W. Peng, I. C. Ni, B. T. Murti, M. L. Tsai and C. I. Wu, *Adv. Sci.*, 2022, **9**, 2201507.
158 N. Tao, Z. Zeng, Y. Deng, L. Chen, J. Li, L. Deng and Y.-N. Liu, *Chem. Eng. J.*, 2023, **456**, 141109.
159 J. Ouyang, C. Feng, X. Ji, L. Li, H. K. Gutti, N. Y. Kim, D. Artzi, A. Xie, N. Kong and Y. N. Liu, *Angew. Chem.*, 2019, **131**, 13539–13544.
160 C. Feng, J. Ouyang, Z. Tang, N. Kong, Y. Liu, L. Fu, X. Ji, T. Xie, O. C. Farokhzad and W. Tao, *Matter*, 2020, **3**, 127–144.
161 X. Wang, X. Sun, T. Bu, K. Xu, L. Li, M. Li, R. Li and L. Wang, *Int. J. Biol. Macromol.*, 2022, **221**, 1558–1571.
162 S. Guo, S. Garaj, A. Bianco and C. Ménard-Moyon, *Nat. Rev. Phys.*, 2022, **4**, 247–262.
163 G. Reina, J. M. González-Domínguez, A. Criado, E. Vázquez, A. Bianco and M. Prato, *Chem. Soc. Rev.*, 2017, **46**, 4400–4416.
164 B. Ma, C. Martín, R. Kurapati and A. Bianco, *Chem. Soc. Rev.*, 2020, **49**, 6224–6247.
165 L. Song, L. Ci, H. Lu, P. B. Sorokin, C. Jin, J. Ni, A. G. Kvashnin, D. G. Kvashnin, J. Lou, B. I. Yakobson and P. M. Ajayan, *Nano Lett.*, 2010, **10**, 3209–3215.
166 B. Radisavljevic, A. Radenovic, J. Brivio, V. Giacometti and A. Kis, *Nat. Nanotechnol.*, 2011, **6**, 147–150.
167 R. Kurapati, K. Kostarelos, M. Prato and A. Bianco, *Adv. Mater.*, 2016, **28**, 6052–6074.
168 R. Kurapati, S. P. Mukherjee, C. Martín, G. Bepete, E. Vázquez, A. Pénicaud, B. Fadeel and A. Bianco, *Angew. Chem., Int. Ed.*, 2018, **57**, 11722–11727.